OBSERVATIONS OF AEROSOL-CLOUD INTERACTIONS WITH VARYING VERTICAL SEPARATION BETWEEN BIOMASS-BURNING AEROSOLS AND STRATOCUMULUS CLOUDS OVER THE SOUTH-EAST ATLANTIC

BY

SIDDHANT GUPTA

THESIS

Submitted in partial fulfillment of the requirements
for the degree of Master of Science in Atmospheric Sciences
in the Graduate College of the
University of Illinois at Urbana-Champaign, 2018

Urbana, Illinois

Advisers:

   Professor Greg M. McFarquhar
   Professor Robert M. Rauber

ABSTRACT

Cloud and aerosol data collected above, within and below clouds from six research flights during the ObseRvations of Aerosols above Clouds and their intEractionS (ORACLES) field campaign in September 2016 were used to determine how the microphysical properties of marine stratocumulus clouds over the South-East Atlantic varied depending on whether overlying biomass-burning aerosols were present immediately above, or separated from cloud tops. Forty vertical cloud profiles were classified into two regimes, Mixing and Separated, according to whether the plume of densest aerosols was mixing into or separated from cloud tops. A statistical analysis showed that more numerous and smaller cloud droplets were sampled in the mixing regime with the median N_c 100 to 150 cm^{-3} higher and the median R_e 1.5 to 2 µm lower than the separated regime. In addition, the median liquid water content (LWC) near cloud base was 0.06 g m^{-3} lower while similar LWC was sampled within cloud and near cloud top the LWC was 0.08 g m^{-3} higher. Inhomogeneous mixing near cloud top led to a decrease in the total number concentration and LWC by up to 28% and 20% respectively and led to an increase in the median volume diameter up to 29 µm for the separated regime. These patterns were observed regardless of the large-scale meteorological conditions. Precipitation suppression was observed during the mixing regime as a lower probability of high drizzle (D > 50 µm) concentration (>0.1 cm^{-3}) was observed during the mixing regime (0.2) compared to the separated regime (0.24).

ACKNOWLEDGEMENTS

To mom and dad.

TABLE OF CONTENTS

CHAPTER 1: INTRODUCTION

Clouds reflect shortwave solar radiation to space cooling the Earth, while absorbing longwave radiation and emitting at lower temperatures than the surface, warming the planet. If the nature of cloud-radiation interactions changes as greenhouse gases increase, there could be large impacts on global climate. For example, a 5% increase in shortwave reflection would compensate for the increase in greenhouse gases (CO_2, CH_4, etc.) since 1750 (Ramaswamy et al. 2001).

Globally, stratocumulus is the most common cloud type with low-lying stratiform clouds covering up to 30% of Earth's ocean surface (Warren et al. 1988). Marine stratocumulus commonly form off western continental coasts in a boundary layer capped by a strong inversion and low clouds can exert a net negative forcing of up to -18 W/m^2 on Earth's radiation budget (Hartmann et al. 1992). The impact of clouds on radiation depends on the number, sizes and phases of cloud particles and their horizontal and vertical distribution. In turn, these properties depend on the numbers, sizes, composition and vertical distribution of aerosols, as well as on meteorological and environmental conditions.

Increases in aerosols acting as cloud condensation nuclei (CCN) can increase cloud droplet concentrations and decrease drop effective radii. Under conditions of constant liquid water content, this would increase cloud optical thickness (COT) and shortwave reflectance (Twomey 1974, 1977). However, COT depends on cloud liquid water content (LWC), depth and droplet sizes, which change with aerosol concentration and composition. COT can also decrease due to reduction of LWCs. Unless the overlying air is humid, LWC in stratocumulus (Ackerman et al. 2004) and ship tracks (Coakley and Walsh, 2002) can decrease with higher droplet

concentrations due to enhanced dry air entrainment (Small et al. 2009; Rosenfeld et al. 2014), weakening the increase in COT associated with smaller droplets. The change in liquid water path (LWP) in polluted stratocumulus can also depend on their diurnal cycle. LWP for polluted clouds is greater during nighttime due to more efficient boundary layer mixing, but decreases faster during daytime due to boundary layer decoupling (Sandu et al, 2008).

The presence of more numerous, smaller droplets in polluted clouds can inhibit drop coalescence, suppressing drizzle formation and precipitation efficiency. This can lead to clouds having higher LWP and longer lifetimes, increasing the shortwave forcing (Albrecht 1989). This assumes a monotonic, inverse relation between precipitation development and droplet concentration. However, precipitation development also depends on boundary layer characteristics such as stability, Convective Available Potential Energy (CAPE), Convective Inhibition (CIN), inversion strength, depth, etc. and its susceptibility to changes in aerosols can depend on effective radius (Rosenfeld et al, 2012) and cloud thickness (Terai et al, 2012). Aerosols can also invigorate convection, resulting in greater liquid water flux to higher altitudes and destabilization aloft due to the additional latent heat release (Koren et al, 2005; Rosenfeld et al, 2008). Further, precipitation susceptibility to aerosols depends on cloud dynamics and regime (Stevens and Feingold, 2009). There is a wide spread in the aerosol effects estimated by Global Circulation Models (GCM), ranging from -3 W m^{-2} to -1 W m^{-2} (Lohmann and Feichter, 2005) and cloud adjustments due to changes in thermodynamics and dynamics contribute the largest uncertainty in quantification of the change in Earth's energy budget (Boucher et al, 2013).

Biomass Burning (BB) aerosols have low single-scattering albedos and directly absorb shortwave solar radiation, exerting a positive radiative forcing at the top of the atmosphere. The associated warming can be amplified if the BB aerosols are present within the cloud, leading to

evaporation of cloud droplets, the so-called semi-direct effect (Hansen et al. 1997; Ackerman et al. 2000). Aerosols above a reflective cloud layer absorb more solar radiation than aerosols present below or within cloud, affecting atmospheric stability and cloud formation and maintenance (Haywood and Shine, 1997). This leads to a complex relationship between vertical aerosol profiles and cloud microphysics, so that both the magnitude and sign of the semi-direct forcing can vary due to an increase or reduction of cloud cover and albedo. For example, Johnson et al. (2004) used a large-eddy simulation (LES) model to show that whether absorbing aerosols were within, above or above and within the boundary layer (BL) had a significant impact on the magnitude and sign of the semi-direct forcing. Aerosols above the BL led to a stronger inversion and decreased entrainment, whereas those within the BL caused evaporation and decoupling of the BL.

According to Koch and Del Genio (2010), absorptive heating from aerosols within cloud can burn off clouds, aerosols below cloud enhance convection and increase cloud cover, and aerosols above cloud stabilize the underlying layer and result in enhanced cloud cover due to reduced entrainment. Because of such effects, aerosols within cloud can have a positive semi-direct forcing, whereas those below cloud could have a negative forcing (McFarquhar and Wang, 2006). Many large-scale models do not adequately consider cloud microphysical responses to the vertical profile of aerosol loading and their evaluation of aerosol effects on clouds has been limited (Hill et al. 2008).

Because meteorological conditions affect cloud evolution, variations in environmental conditions also have an impact on how aerosols impact cloud properties. Aerosol loading is strongly governed by meteorological parameters such as wind speed, boundary layer stability and air-mass history. Changes in the environment produced from changes in thermodynamic profiles and

cloud microphysics, in response to aerosol direct, semi-direct and indirect effects, can buffer or offset aerosol effects on clouds (Stevens and Feingold, 2009). Morrison and Grabowski (2011) showed that such changes in convection and cloud microphysics can feed back into cloud dynamics and microphysics, which then feed into cloud impacts on aerosols, which in turn affect cloud properties. Wet removal of absorbing aerosols by precipitation below cloud also affects these interactions (Rosenfeld et al, 2014).

Satellite-based studies (Brioude et al. 2009; Chand et al. 2009; Constantino and Breon, 2013) have had difficulties quantifying cloud-aerosol interactions because of concerns about the accuracy of aerosol and cloud retrievals (Painemal and Zuidema, 2011), especially in locations where clouds are overlaid by aerosols (Haywood et al. 2004; Coddington et al. 2010). Although co-incident in-situ observations of aerosol characteristics and cloud properties exist (e.g., Durkee et al, 2000; McFarquhar and Heymsfield, 2001; Twohy et al, 2005), they have not adequately characterized the varying aerosol vertical structure and co-incident cloud properties. Such observations are needed to evaluate biases in remote sensing retrievals and better understand the aerosol effects and the associated feedbacks.

The ObseRvations of Aerosols above Clouds and their intEractionS (ORACLES) project provides such airborne observations in the South-East Atlantic. Large aerosol optical depths overly a permanent stratocumulus cloud deck between July and October, serving as a natural laboratory for studying above-cloud aerosols and their interactions with clouds. Aerosols originating from biomass burning in Southern Africa are initially located at altitudes between 2000 and 5000 m and descend and mix into the cloud with advection from the background westerlies off the coast of Africa (Haywood et al. 2004). The aerosol-cloud interactions introduce inter-model differences in the climatic effects of aerosols and induce biases in satellite

retrievals of clouds (Haywood et al, 2004) and aerosols in their vicinity (Wen et al, 2008; Marshak et al, 2008).

Overall, ORACLES' science goals include determination of the evolution and seasonal variation in aerosol properties and their vertical location, constraining aerosol-induced heating rates and their impact on cloud structure, and surveying the aerosol mixing into the BL and measuring the changes affected in cloud microphysics (Redemann, 2014). This paper presents in-situ observations of cloud microphysical properties from the marine stratocumulus over the South-East Atlantic and their response to the overlying layer of aerosols according to the separation between the aerosol-cloud layers. The understanding gained from quantifying relationships between cloud and aerosol properties in this environment, where few previous in-situ observations exist, hence contributes to understanding aerosol indirect effects in a unique meteorological environment where variation in vertical locations of aerosols with respect to the cloud exists.

The remainder of this thesis is organized as follows; Chapter 2 presents the instruments used to make these observations and describes their calibration and data quality. Chapter 3 shows a case study on cloud observations made during the 6 September 2016 flight. A statistical analysis in Chapter 4 categorizes the measurements from the case study and five other research flights into different regimes based on the vertical separation between aerosols and clouds, and the aerosol concentration. Chapter 5 summarizes the principal findings and offers directions for future work.

CHAPTER 2: INSTRUMENTATION AND DATA QUALITY

In-situ and remote sensing data acquired during ORACLES 2016 are used to investigate how cloud properties change depending on the amount of mixing of aerosols into cloud top. The first Intensive Observation Period (IOP) for ORACLES was based out of Walvis Bay, Namibia between 27 August and 27 September 2016. The NASA P-3 and ER-2 aircraft used during ORACLES 2016 flew west of the African coast between 1° W to 15° E and 5° S to 25° S. The NASA P-3 aircraft was equipped with in-situ probes for measuring aerosol and cloud properties, along with remote sensing instruments for radiative measurements and aerosol and cloud retrievals.

The P-3 data from several probes are used in this study. For measuring the droplet number distribution function n(D), the P-3 was equipped with a Cloud and Aerosol Spectrometer (CAS) measuring particles with maximum dimension (D) between 0.51 to 50 µm (Baumgardner et al. 2001), a 2D-Stereo probe (2D-S) nominally sizing particles with 10 µm < D < 1280 µm (Lawson et al. 2006), a Cloud Imaging Probe (CIP) for 25 µm < D < 1600 µm (Baumgardner et al. 2001), and a High Volume Precipitation Sampler (HVPS-3) for 150 µm < D < 1920 µm (Lawson et al. 1998). The P-3 was also equipped with a Cloud Droplet Probe, CDP which became unaligned due to a loose screw and hence its data are unusable for this campaign.

Bulk liquid water content (LWC) was measured by a King hot wire (King et al. 1978) and a hot wire probe installed as part of the Cloud, Aerosol, and Precipitation Spectrometer (CAPS) which also consisted of the CIP and CAS. An Ultra-High Sensitivity Aerosol Spectrometer (UHSAS) measured the aerosol n(D) for 0.06 < D < 3 µm (Cai et al. 2008) and a Passive Cavity Aerosol Spectrometer Probe (PCASP) measured the aerosol n(D) for 100 nm < D < 3 µm (Strapp et al.

1992). The Turbulent Air Motion Measurement System (TAMMS) measured wind speeds at a temporal resolution of 20 Hz. Bulk sub-micron aerosol composition was measured at 0.2 Hz by an Aerodyne Time of Flight Aerosol Mass Spectrometer (ToF-AMS) and Aerosol Optical Depth (AOD) above the location of the aircraft was retrieved at 1 Hz by the Spectrometer for Sky-Scanning, Sun-Tracking Atmospheric Research (4STAR) on board the NASA P-3. Data collected by the P-3 included temperature measured using the aircraft Rosemount 102 total temperature sensor, dew point measured using an EdgeTech 137 chilled-mirror hygrometer and latitude and longitude measured by an inertial navigation system.

Baumgardner et al. (2017) discuss how the cloud probes used in this study function, along with their strengths and limitations. McFarquhar et al. (2017) summarize the basic algorithms used to process data from these probes. This section describes the methodology for combining data from these probes into a single product for characterizing cloud properties, along with the associated calibrations, data checks and quality controls conducted.

Data from the CAPS, namely the CAS, CIP and hot-wire probes are not available before PRF05, the fifth P-3 research flight on 06 September 2016, because the electronics board was improperly seated before that time. This, combined with the failure of CDP during ORACLES 2016, meant that no information on n(D) for droplets with D < 50 µm was available for the first four flights. Hence, data from these flights are omitted from subsequent analyses.

Calibration of the PCASP and CAPS probes was performed at Droplet Measurement Technologies, Inc., before the Intensive Observation Period (IOP). The PCASP was calibrated by passing polystyrene latex (PSL) beads, room air and filtered air through the inlet of the probe, while the CAPS was calibrated using PSL and glass beads. Cleaning and electronic maintenance of the CAPS was also performed. Power terms for the King hot-wire needed to calculate the

LWC were calibrated by relating the dissipated heat loss to the analog output voltage according to the energy equations described by King et al. (1978).

Calculation of n(D) from data collected by cloud probes requires the best possible estimate of true air speed (TAS) entering the probe sample volume. There are uncertainties in TAS because the air flow into the probes may differ from the TAS measured by the aircraft system probe mounted on the fuselage. This can occur due to compression of air ahead of the probes (e.g., Weigel et al. 2016) or due to perturbations of the air flow at specific locations around the aircraft induced by flow around the aircraft itself. Although mounting clouds probes on struts attached to the wings is regarded as best practice (Afchine et al. 2017), the location of the ORACLES probes directly underneath the wing of the NASA P-3 (Figure 1) rather than slightly ahead of its leading edge as on the NOAA P-3 (e.g. McFarquhar et al. 2007), suggests the air flow around the wings could have affected cloud sampling by the probes.

A Pitot tube alongside the CIP measured TAS, which was about 20% lower than the system TAS. Although there is some uncertainty if this TAS measurement from the CAPS accurately represents the flow through the instruments (Lance et al. 2010, Johnson et al. 2012), this TAS is used to process data from the PCASP, CAPS and King hot-wire in the absence of any better information. The Airborne Data Processing and Analysis, ADPAA processing package (Delene, 2011) was used to process these data using the CAPS TAS. The 2D-S and HVPS-3 data were processed with the system TAS using the University of Illinois/Oklahoma Optical Probe Processing Software (UIOOPS, McFarquhar et al. 2017) because no measurement of the TAS at the location of those probes is available.

Droplets shadow elements of a photodiode array on optical array probes (OAPs, i.e., CIP, 2D-S, HVPS-3) when passing through the probe sample volume, causing a reduction in the laser power

detected by the photodiode receivers. If aerosols deposit on a probe's optical lenses, false identification of droplets can occur due to a stuck or continuously shadowed diode. Because frequent flights through plumes of absorbing aerosols occurred during ORACLES 2016, aerosols did deposit on the optical lenses of these probes, leading to a degradation of probe performance during the course of flights. To minimize the impact from these stuck bits, all lenses were carefully cleaned with isopropyl before each flight. Further, the voltages across probe photodiodes were monitored during flights. If the voltages decreased due to aerosol deposition, the laser power was reset, and the stuck bits masked so that data from that photodiode were ignored.

The 2D-S probe was tested at the Stratton Park Engineering Company, SPEC laboratory after the IOP and aerosol deposition was observed on the inside of the receive side mirror for the vertical channel (Figure 2). This led to decreased diode voltages during the experiment and hence only data from the horizontal channel are used in this analysis. Although the voltages from the horizontal channel were higher (e.g., between 1 and 2.5 V), there were time periods when some of the bits were masked and images that did not represent real particles (henceforth artifacts) were still recorded. To eliminate these artifacts, data from stuck diodes (i.e. diodes shadowed for more than 20% of the flight time) are ignored. After removing these diodes, there are still particles with D>50 µm that appear due to stuck diodes and these artifacts (Figure 3a) are rejected using an aspect ratio threshold of 4. An area ratio (Heymsfield and McFarquhar 1996, the projected area of a particle divided by the area of circle with diameter equal to the maximum dimension of the particle) threshold of 0.5 is also used to reject the elongated particles seen in Figure 3b that are indicative of multiple stuck diodes.

Artifacts associated with the generation of artificially high number of small ice crystals by the shattering of large ice crystals on probe tips have been observed in past studies. While processing OAP data, these artifacts are typically identified as particles that have times between their arrival in the probe sample volume (henceforth inter-arrival times) less than some threshold (e.g., Field et al. 2003, 2006). Although ice particles were not sampled during ORACLES 2016, an analogous approach is used to reject any particles that have interarrival times less than 6 µs as this is indicative of intermittently stuck diodes (Figure 3c). The thresholds and criteria used for determining these artifacts were chosen after careful examination of several particles and tests of varying thresholds. Out-of-focus hollow particles (Figure 3d) are accepted if they pass the rejection criteria and are reconstructed according to the Korolev (2007) algorithm.

Fifteen P-3 research flights (PRFs) were conducted during ORACLES 2016 representing a total of 108 flight hours. The temporal resolution of the collected data is 10, 10 and 25 Hz for the CAPS, PCASP and King hot-wire, respectively, which are averaged to 1 Hz, corresponding to a spatial resolution of approximately 150 m as dependent on the TAS. Throughout this study, a cloud is defined as $N_c > 10$ cm^{-3} and LWC > 0.05 g m^{-3} (Lance et al. 2010, Bretherton et al. 2010a). Data from six flights when at least 1000 s were spent in cloud and at least three maneuvers were conducted to examine the vertical variation of cloud properties (Table 1) are analyzed. Cloud sampling included ascents or descents through cloud along a constant heading, henceforth called vertical cloud profiles, sawtooth profiles (ramped legs starting above or below cloud, including a series of ascents and descents through cloud) and level legs through cloud.

The total droplet concentration N_c, effective radii R_e and liquid water content LWC are determined by merging CAS size distributions for cloud droplets with diameters between 3 and 50 µm and 2D-S size distributions for diameters between 50 and 1280 µm. Droplets with D >

1280 µm measured exclusively by the HVPS-3 had very low concentrations (droplets with D>1280 µm were observed only during three cloud legs, and for less than 10 s during those legs) and hence are not included in the quantitative analysis.

Closure tests comparing the bulk LWC against that derived from the merged n(D) assess the data quality and check for calibration shifts during the experiment. Because the King hot-wire has reduced response for diameters below 12 µm and above 40 µm (Biter et al. 1987, Strapp et al. 2003), the bulk LWC is compared against the LWC derived by integrating the droplet mass distribution for 12.5 < D < 40 µm. These measurements were strongly correlated with R=0.77 and a best-fit slope = 0.65 across the six flights. Figure 4 shows the scatter plot comparing the LWC measurements on PRF13 where each point represents a 1 s average, colored by the droplet concentration for 12.5 < D < 40 µm. The King hot-wire has a sensitivity of 0.02 g m^{-3} with 5% accuracy at 1 g m^{-3} (King et al. 1978) and data points with King LWC < 0.05 g m^{-3} are removed.

Throughout this study, D > 3 µm is used as the size threshold for defining cloud droplets. When the bulk LWC was compared against the LWC derived by integrating the mass computed from the droplet size distributions for D > 3 µm, the correlation between the measurements decreased by 11% on average from that computed using 12.5 < D < 40 µm (Table 2). The LWC estimated from the size distribution with D > 3 µm overestimated the King LWC for up to 30% of the time. This is most likely because the hot-wire has a decreased collision efficiency for smaller droplets. In fact, these overestimates were most common whenever the concentration for drops with D < 12.5 µm, N(D<12.5) was greater than 400 cm^{-3}. For times with N(D<12.5) > 400 cm^{-3}, the LWC from the size distributions with D > 3 µm overestimated the King probe LWC by 60%, averaged over all six flights.

CHAPTER 3: CASE STUDY: 6 SEPTEMBER 2016

3.1.   FLIGHT TRACK AND MODULES

Figure 5 shows a Spinning Enhanced Visible and Infrared Imager (SEVIRI) visible image of the cloud field over the southeast Atlantic at 14.00 UTC on 6 September 2016. The flight track for the fifth P-3 research flight (henceforth, PRF05) is overlaid. Locations of the sawtooth profiles, termed S1 to S4 in chronological order, and individual vertical profiles through cloud, P1 to P4, are also indicated. This section examines data collected during these vertical profiles together with in-situ and remotely sensed aerosol data collected immediately before and after the profiles to characterize the relationship between aerosol and cloud properties. This flight was designed to explore cloud-aerosol interactions. Although the ER-2 did not operate on this day, PRF05 is chosen for detailed analysis because it included more time sampling clouds than other flights.

Figure 6 shows the altitude flown by the P-3 as a function of time for PRF05, colored by the aerosol concentration (measured by the PCASP for accumulation-mode aerosols, $0.1 < D < 3$ µm) N_a. The PCASP N_a was, on average, a factor of 2 less than the concentration measured by the UHSAS, with the number distribution function, n(D) below 300 nm especially underestimated by a factor of 3 to 5 (Figure 7). It is suspected that the PCASP was biased low compared to the UHSAS because the total concentrations measured by the PCASP on the NASA P-3 were lower on average than those measured by the PCASP on the BAe146 on 18 August 2017 during the second phase of ORACLES by about a factor of 3, similar to the difference with the UHSAS. Thus, due to the uncertainty in PCASP N_a, the values should not be used quantitatively but can still be used to compare aerosol concentrations in different locations for identification of the location of the aerosol plume.

A flight module consisting of four legs flown between 08:20 and 09:00 UTC consisted of the following components: a 10-min constant altitude leg (L1) starting at 08:20 UTC at about 150 m above the ocean surface to sample aerosols in the marine boundary layer (MBL); after ascending through the boundary layer, a constant altitude leg (L2) at 850 m sampling clouds in-situ for 10 min ending at 08:40 UTC; a 5-min leg (L3) about 100 m above cloud top, at 1100 m, starting at 08:41 UTC, enabling retrieval of above-cloud Aerosol Optical Depth (AOD) with 4STAR and in-situ sampling of aerosols with the PCASP, UHSAS and AMS; and a sawtooth pattern (S1) between 08:46 and 08:57 UTC, when multiple vertical profiles were flown from approximately 200 m below cloud base to 100 m above cloud top, to document changes in cloud microphysical properties with height.

A similar module was repeated three more times during the flight, with slight variability in the duration of each leg. These modules can be seen in Figure 6 between 09:50 and 10:20 UTC, 10:20 and 11:20 UTC, and 12:40 and 13:30 UTC. These modules were separated by other legs, such as vertical profiles through the overlying biomass burning aerosol plume (e.g., between 09:00 and 09:05 UTC) and constant altitude legs through the level of maximum aerosol concentration observed during the profile (e.g., between 09:05 and 09:25 UTC at 2500 m). Individual profiles sampling clouds, P1 to P4, were flown when sampling the atmospheric column between the MBL and the aerosol plume. The timing of these profiles used to identify the vertical locations of the cloud and aerosol layers are listed in Table 3.

S1 and S2 were conducted when the P-3 was heading north, and S3 while heading south, all along 9E in closed cells of optically thick marine stratocumulus (Figure 5). S4 was conducted later in the day, between 13:15 and 13:30 UTC, and closer to the coast, while heading southeast in optically thinner stratocumulus. The range of cloud optical thickness (COT) retrieved by the

13

MODerate-resolution Imaging Spectroradiometer (MODIS) on board the Aqua satellite at 13 UTC (worldview.earthdata.nasa.gov) is consistent with COT calculated by integrating the cloud extinction derived from the merged CAS and 2D-S size distribution (Table 3). The presence of high clouds restricted the COT retrieval for S1.

3.2.   MESOSCALE FEATURES

Figure 8 shows the European Centre for Medium-Range Weather Forecasts (EMCWF) reanalysis for mean sea level pressure, 500mb geopotential height and surface wind at 12:00 UTC on 6 September 2016 and Figure 9 shows the reanalysis for boundary layer height, and relative humidity (RH), geopotential height, and winds at 925mb. South-southeasterly winds with wind speeds between 5 and 8 m s^{-1} were observed at the surface and at 925mb, associated with a low-pressure system at the surface, east of the study region, centered at 17° S and 13° E. This wind resulted in advection of the low-level clouds toward the northwest during the day. SEVIRI images show open- and closed-cells of stratocumulus occurring over the study region. Closed cells are typically observed when warm air overlies colder ocean water while open cells are typically observed where cold air overlies warmer water (Comstock et al. 2005). Due to the advection of cold, dry continental air from the southeast, a thinner boundary layer was sampled closer to the coast (Figure 9). This led to cloud thinning, especially south of 19° S, where open cellular structure was observed, and optically thinner stratocumulus clouds were sampled during S4. A positive gradient in 500mb geopotential heights and RH toward the north, suggests warmer air was present where closed cellular structures were sampled, e.g., during S2 and S3. Pockets of open cells (POCs) were observed in the study region, persisting throughout the day. S1 and S2 were flown within closed cells while S3 was flown near a POC boundary, however, the clouds sampled during S3 lied outside it, and within a closed cell.

14

3.3. AEROSOL COMPOSITION AND AIR-MASS HISTORY

The National Oceanic and Atmospheric Administration Hybrid Single Particle Lagrangian Integrated Trajectory (NOAA HYSPLIT) model (Stein et al. 2015) is used to generate back-trajectories shown in Figure 10 using the National Center for Environmental Prediction Global Forecast System (NCEP GFS) model fields. Altitudes selected for these back-trajectories for S1, S2 and S3 correspond to cloud base and top heights (500 m and 1000 m) and 2500 m, the latter corresponding to the location of constant altitude legs (e.g., between 11:40 and 11:50 UTC) flown to sample a layer of high aerosol concentration (Figure 6). N_{am} shown in Figure 11 are obtained from the NASA Global Modeling and Assimilation Office Goddard Earth Observing System Model Version-5 (GMAO GEOS-5) reanalysis valid at 12:00 UTC at 925mb.

Figure 10 shows five-day back-trajectories for S1 to S3, ending at 10:00 UTC, and for S4 ending at 13:00 UTC (since S4 was flown later in the day) on 6 September 2016. Figure 11 shows the N_{am} reanalysis for dust and organic carbon (OC) at 925mb height, adjacent to cloud tops for S1, S2 and S3, and 300 m above cloud tops for S4. Figure 12 shows in-situ sampled N_{am} for organic carbon (OC), ammonium (NH_4^+), nitrates (NO_3^-) and sulfates (SO_4^{2+}) as a function of height, measured by the AMS, for one select profile during each of the sawtooths. Figure 13 shows the total N_{am} measured by the AMS as a function of altitude for all aerosol types combined for the same profiles. Figure 14 shows N_{am} based on aerosol type, sampled in-situ using the AMS as a function of the aircraft altitude and time during PRF05.

The air-masses near cloud base and top for S1 were both advected from the MBL in the southeast (green, Figure 10a, b). The N_{am} reanalysis showed high dust and low OC near cloud top, and the in-situ sampling found decreased N_{am} (<5 µg m^{-3}, Figure 13) relative to below cloud base, comprising of OC (<5 µg m^{-3}) and SO_4^{2-} (<2 µg m^{-3}), shown in Figure 12. The air-masses

15

below cloud base for S1, S2 and S3 originated in the MBL southeast of the study region (Figure 10a) and the sampled air had low N_{am} (<10 µg m^{-3}, Figure 13), primarily comprising of OC and SO_4^{2+}. While the air mass originated in the MBL for S4 as well, it was advected from the east and observed to have lower N_{am} (<2 µg m^{-3}) compared to other profiles. For each sawtooth, the air mass below cloud base originated from the MBL, advected from the southeast of the study region by the southeasterly surface winds and did not originate over the African continent.

Near cloud tops, aerosol composition and N_{am} varied between profiles based on the air-mass back-trajectory and source region. When the air-mass originated from the African continent, i.e., for S2 and S3 (Figure 10b), higher N_{am} (20 to 40 µg m^{-3}) was sampled, primarily consisting of OC (20 to 30 µg m^{-3}) and SO_4^{2-} (5 to 10 µg m^{-3}) with traces of NH_4^+ and NO_3^-, less than 3 µg m^{-3}. In addition, the reanalysis showed negligible dust (<5 µg m^{-3}) and higher OC (15 to 30 µg m^{-3}). In comparison, the air mass near cloud top for S1 originated from the MBL in the southeast. Lower N_{am} (<5 µg m^{-3}) was sampled, primarily consisting of comprising of OC (<5 µg m^{-3}) and SO_4^{2-} (<2 µg m^{-3}), with the GEOS-5 reanalysis showing higher dust N_{am} (15 to 25 µg m^{-3}) with negligible OC (<5 µg m^{-3}, Figure 12). In case of S4, the air mass above cloud top originated from the MBL but likely underwent mixing with the aerosol plume as suggested by the trajectory and aerosol composition.

Aerosols above cloud tops, originating from the African continent, represent biomass burning products, comprising of high OC. Maximum values of aerosol concentration (measured by the PCASP for accumulation-mode aerosols, 0.1 < D < 3 µm) N_a, were sampled during constant altitude legs at about 2500 m, e.g., between 09:00 and 09:30 UTC after S1, between 11:30 and 12:00 UTC after S3, and between 13:30 and 14:00 UTC after S4 (Figure 6). The back-trajectories from S3 and S4 suggest the aerosols at this altitude originated from the African

16

continent (Figure 10 c, d) and the aerosol composition is dominated by OC (Figure 14). Although, the air-mass at 2500 m, above S1, advected from the west of the study region (green, Figure 10c), the aerosol composition is similar to that above S3 and S4 (OC > 20 µg m^{-3} with 5 < SO$_4^{2-}$ < 10 µg m^{-3}), suggesting this air-mass underwent mixing with the aerosol plume and had more aged aerosols compared to the other profiles.

The aerosol composition and mass concentration (N$_{am}$) for an air mass depend on its trajectory and source region. Air-mass history determined using back-trajectories explains the variation observed between sawtooth profiles in both above-cloud (reanalysis and in-situ) and below-cloud (in-situ) aerosol composition and N$_{am}$. Further, air-mass history was combined with aerosol composition to determine the aerosol source. Similar aerosol composition, indicative of biomass burning products, was sampled above cloud tops for S2, S3 and S4. The aerosol composition below cloud base differed from that above cloud tops and it was observed that biomass burning aerosols were not present below cloud base during these profiles.

3.4.   SAWTOOTH PROFILES AND REGIME CLASSIFICATION

Figure 15 shows the P-3 altitude as a function of time for the four sawtooth profiles, S1, S2, S3 and S4, colored by the King LWC. For example, six individual profiles were obtained during S4 and labeled as '4a', '4b', etc. These profiles lasted between 90 and 150 seconds each, corresponding to a horizontal distance between 10 and 17 km and a vertical ascent/descent rate of 5 m/s during each profile. Cloud base and cloud top are identified as the minimum and maximum altitude satisfying the criteria identified to define cloud (LWC > 0.05 g m^{-3} and N$_c$ > 10 cm^{-3}). The thickness of the cloud deck, ΔZ, is then calculated and ranged between 207 and 281 m, giving an average thickness of 245 m (Table 3). The clouds sampled during S4 in the open cells were thinner and lower (cloud base below 300 m) than those sampled during S1 to S3

17

(cloud base above 500 m) because cold air advection (Figures 8 and 9) led to a deeper boundary layer further north and away from the coast.

Figure 16 again shows the altitude flown during S1, S2, S3 and S4 (and two minutes before and after), except this time the points are colored by the PCASP N_a. The N_a for time periods identified as in-cloud are not shown because of the potential for contamination by cloud droplet shattering during these periods. Using the cloud base and top identified using the cloud thresholds, a vertical gap of about 200 meters is identified between the cloud deck and the level of enhanced $N_a > 100$ cm^{-3} overlying the cloud deck for S4, but not for S1, S2 and S3. This indicates that the two layers were separated during S4 and hence it was unlikely that a lot of aerosols were mixing into cloud from above.

Figure 17 shows N_c and PCASP N_a measured during the fifth vertical profile for S1 to S4, as a function of altitude. The blue dashed lines indicate cloud base and top, and the red dashed line indicates 100 cm^{-3}. Each point represents a 1s average, or approximately 150 m. For the fifth profile on S1, S2 and S3, $N_a > 100$ cm^{-3} adjacent to the cloud top showing a thicker plume of aerosols is mixing into the cloud deck than for S4 when $N_a < 20$ cm^{-3} was immediately adjacent to cloud top. The maximum AOD retrieved by 4STAR within five minutes before and after a cloud profile, are averaged and listed in Table 3. With a TAS of 150 m/s, this represents the maximum AOD measured within 45 km of the cloud horizontally. The AOD for sawtooth 4 (0.41) suggests that although the aerosol concentrations were very low immediately above cloud tops, the aerosol plume was present above the cloud deck and separated from it. This is also supported by the in-situ measurement of $N_a > 100$ cm^{-3} about 200 m above cloud top during S4. Similar observations from other profiles during the sawtooth legs show mixing of a heavy plume of large aerosol concentrations at cloud top for S1, S2 and S3, and separation between layers for

18

S4. The first three sawtooth profiles flown in PRF05 are hence categorized as "mixing" since a heavy aerosol plume is likely being entrained into cloud top while sawtooth 4 is categorized as "separated" since no aerosols with concentrations greater than 100 cm^{-3} are adjacent to within 100 m of cloud top, and hence are unlikely to be mixed in.

3.5.   VARIATION IN CLOUD PROPERTIES WITH HEIGHT

Trends in the change in N_c, R_e and LWC calculated from the merged CAS and 2D-S size distributions with height, observed during the vertical profiles from PRF05, are shown in Figures 18, 19 and 20. Initially, N_c increases with height above cloud base as droplet nucleation occurs within updrafts, and as droplets continue to ascend, fewer nucleate as the supersaturation ceases to increase and hence the critical supersaturation of smaller droplets is not reached. There are some fluctuations due to mixing and occasional nucleation events. The R_e and LWC increase with height due to the condensational growth of droplets and the collision-coalescence process.

During some of these profiles (e.g., S1d, P1, P3), a large variation in N_c and R_e was observed near cloud base for small LWCs. For S1d, this layer extended from 550 to 680 m and the vertical change in cloud properties for this profile is further examined in Figure 21. N_c increased from 10 cm^{-3} at 550 m to about 600 cm^{-3} at 600 m and varied between 200 and 600 cm^{-3} up to 680 m. The R_e decreased from 14 µm at 550 m to about 4 µm at 600 m and varied between 3 and 8 µm up to 680 m. Small LWCs (< 0.05 g m^{-3}) were sampled up to 600 m and varied between 0.05 and 0.1 g m^{-3} up to 680 m. Figure 22 shows the size distribution for this profile as a function of altitude. Large cloud droplets (D > 20 µm) were observed between 600 and 680 m with a number distribution function greater than 0.1 cm^{-3}, suggesting this layer was associated with larger cloud droplets falling out of cloud since its unlikely these droplets formed near cloud base. The number distribution function for droplets with 3 < D < 8 µm, n(3< D < 8 µm) was close to 100 cm^{-3}

between 600 and 680 m and decreased to about 10 cm^{-3} below 600 m. This suggests droplet scavenging by the precipitating droplets, causing the decrease in N_c and increase in R_e below 600 m. Condensational growth of droplets with $D < 10$ µm above 680 m can be seen in Figure 22 and combined with the collision-coalescence process, led to the formation of larger droplets ($D > 20$ µm) which then fall out.

During each cloud profile, N_c and LWC decreased near cloud top (Figures 18 and 20) likely due to the entrainment of dry air and subsequent mixing of sub-saturated air into the cloud. Previous studies (Burnet and Brenguier, 2007; Lu et al., 2011) have described two models for entrainment-mixing processes near cloud top, namely, homogeneous and inhomogeneous mixing, and found inhomogeneous mixing within stratocumulus clouds. These models are based on the relative time scales for droplet evaporation and homogenization of a diluted cloud volume. When mixing between droplet-free air and the cloudy air occurs slowly, droplets surrounding the sub-saturated air evaporate completely. Meanwhile, the remaining cloud droplets maintain their size as the diluted air moistens due to droplet evaporation. Consequently, N_c decreases but the mean volume diameter (D_v) remains unchanged and hence a plot in the $N_c - D_v$ phase shows a range of N_c values for relatively unchanging D_v. This process is termed as inhomogeneous mixing.

Figure 23 shows D_v for each profile plotted as a function of N_c, for the upper half of the cloud deck. During S1, S2, P1 and P4, similar D_v were measured for N_c ranging from 10 to 1000 cm^{-3} indicating inhomogeneous mixing. However, a negative D_v-N_c correlation was observed for the remaining profiles as D_v increased when N_c decreased, e.g., during S3, $10 < D_v < 15$ µm was measured for $N_c > 200$ cm^{-3} while D_v up to 20.5 µm was measured for $N_c < 200$ cm^{-3}. Figures 24 and 25 show the size distribution for P1 and P3 respectively, as a function of altitude.

20

Inhomogeneous mixing was observed during P1 and the concentration for smaller droplets, n(D < 10 µm) decreased above 750 m, and the concentration for larger droplets, n(D > 20 µm) decreased above 800 m. In contrast, during P3, only the smaller droplets evaporated, as n(D < 10 µm) is observed to decrease above 800 m, while the concentration of larger droplets (D < 10 µm) increased. Consequently, a negative D_v-N_c correlation was observed for this profile.

Past studies (e.g., Burnet and Brenguier (2007), Lehmann et al. 2009) have explained the negative D_v-N_c correlation as a continuation of the inhomogeneous mixing process, termed as "inhomogeneous entrainment mixing with subsequent ascent" (Lu et al., 2011). As the diluted cloud volume undergoes lifting, larger cloud droplets grow faster due to decreased competition for water vapor made available by droplet evaporation. This is supported by the observation of n(D > 20 µm) increasing above 850 m during P3, while n(D > 20 µm) was decreasing above 800 m during P1.

CHAPTER 4: STATISTICAL ANALYSIS OF MULTIPLE FLIGHTS

Two types of flights were conducted during ORACLES 2016, routine flights (RF) and target-of-opportunity flights (TF). During RFs, the NASA P-3 would take off from Walvis Bay, Namibia and fly in a northwest direction toward 10˚S, 0˚E, returning along the same path. The purpose of these flights was to study the spatial extent and aging of the aerosol plume advected westward off the African coast along with its effect on the underlying clouds (Redemann, 2014). During TFs, a different flight track was flown depending on meteorological conditions and flight objectives. A statistical analysis is used in this chapter to determine how the change in the vertical location of biomass burning aerosols above cloud tops is correlated with the change in microphysical properties of the clouds.

Data from six flights when at least 1000 s was spent in cloud and at least three cloud profiles examining the vertical variation of cloud properties were conducted (Table 1) are analyzed. The flights were flown on 6, 10, 12, 14, 20 and 25 September 2016 and include three RFs and three TFs. The total flight time across the flights was 49.8 hours which included 4 hours of in-situ cloud sampling (Table 4). Forty cloud profiles flown between 10° S to 20° S and 0° to 12° E were identified from these flights and Figure 26 shows the six flight tracks with the locations of the cloud profiles.

Forty cloud profiles from the six flights were categorized into one of two regimes, mixing and separated, as described in Chapter 3. The altitude flown by the aircraft plotted as a function of time, and the droplet and aerosol concentrations (N_c and N_a) measured before, during and after each profile, were used to identify the vertical location of the heavy aerosol plume relative to the cloud deck, as shown in Figure 16 from PRF05. N_c and N_a profiles plotted as a function of

altitude (Figure 17) were also used to identify profiles with enhanced aerosol concentration (N_a > 100 cm^{-3}) adjacent to cloud tops. For profiles with N_a > 100 cm^{-3} within 100 m above cloud tops, it is likely that the heavy plume of aerosols entrained into the cloud tops and hence these profiles were categorized as "mixing". Sixteen "mixing" profiles were identified from four different flights, and the remaining twenty-four profiles were categorized as "separated", with at least one "separated" profile sampled during each flight, except during PRF11 (Table 4).

Of the forty cloud profiles analyzed, only two profiles had AOD below 0.25 (0.14 for P1 from PRF05 and 0.1 for P1 from PRF07), which suggests the aerosol plume was present above the cloud deck during all other profiles, regardless of its vertical location or separation from the cloud deck. Consequently, profiles with low (less than 100 cm^{-3}) aerosol concentration up to 100 m above cloud tops are categorized as "separated".

Meteorological conditions similar to PRF05 were observed during PRFs 7, 8 and 9. As described in the previous chapter, south-southeasterly winds were observed at the surface and 925mb height, associated with a surface low-pressure system, east of the study region over the continent. Surface wind speeds were between 5 to 10 m s^{-1}, depending on the pressure gradient between the surface-low and a surface-high, located south-west of the study region over the ocean. A region of low RH at 925mb height was observed, closer to the coast, due to the advection of dry continental air into the study region. Because the meteorological conditions were similar on these four flights, any differences in the vertical profiles of cloud properties can be attributed to local differences in aerosol properties and local environmental conditions such as humidity, updraft velocity, stability, and inversion strength and height.

The RF flown on 10 September 2016 (PRF07) included seven vertical cloud profiles and one sawtooth profile. These profiles were flown between 16° S 6° E and 14° S 4° E between 10 and

13 UTC. The AOD above cloud measured by 4STAR was greater than 0.25 before or after all profiles, except for profile 1, which had an AOD of 0.1. This suggests an aerosol plume was present above all profiles, except for the first. For each of these profiles, the PCASP N_a profiles (like Figure 17) suggest the aerosol concentrations adjacent to cloud tops were below 100 cm^{-3}, and hence the aerosol plume was separated from the cloud deck. Therefore, the eight profiles from this flight are categorized as "separated".

The RF flown on 12 September 2016 (PRF08) included two vertical cloud profiles and one sawtooth profile. These profiles were flown between 9.5° and 13° S and 0° and 3° E between 11 and 12.30 UTC. The AOD calculated for the profiles were 0.29, 0.3 and 0.3, suggesting that an aerosol plume was present above the clouds sampled. The N_a was greater than 300 cm^{-3} adjacent to cloud top for the first vertical profile, suggesting the plume was mixing into the cloud and hence this profile was categorized as "mixing". For the sawtooth, and the second vertical profile, low aerosol concentrations were observed adjacent to cloud top. Because $N_a < 100$ cm^{-3} for at least 100 m above cloud tops for these cases, they are categorized as "separated".

The objective for the TF flown on 14 September 2016 (PRF09) was to collect radiative measurements closer to the coast. The flight track (black, Figure 26) comprised of two meridional legs, flown between 16° and 18° S, along 7.5° E and 9° E. Eight vertical cloud profiles were flown during the flight with three profiles between 16° and 17° S along 7.5° E, and five profiles between 17° and 18° S along 9° E. The AOD calculated for the profiles ranged between 0.3 and 0.4. Twelve vertical profiles through the aerosol layer were flown during this flight. $N_a > 100$ cm^{-3}, indicative of polluted conditions, was sampled only above 2000 m above sea level with cloud tops below 1000 m above sea level for each profile. Therefore, all eight profiles from this flight were categorized as "separated".

A TF was flown on 20 September 2016 (PRF11) with the objective of collecting radiative measurements. The flight track (magenta, Figure 26) was similar to the PRF09 flight track wherein two meridional legs were flown, between 15° and 17° S, along 9° E and 10.5° E. Six vertical cloud profiles and one sawtooth profile were flown. The first four profiles were flown between 15.5° and 16.5° S along 10.5° E while the sawtooth and two other profiles were flown between 16.5° and 17.5° S along 9° E. Westerly surface winds associated with the surface-low which extended west of the African coast along with greater 500mb geopotential height were observed along the two meridional flight legs. At 925mb, easterly winds were observed along the flight legs, associated with a low-pressure system toward the north. Consequently, warmer air near the surface was overlaid by dry, polluted continental air in the study region, leading to a thick cloud deck with large aerosol concentrations (up to 600 cm^{-3}) above cloud tops (940 to 950mb). The AOD measured for these profiles ranged between 0.48 and 0.58. A vertical profile was flown through the aerosol plume before each cloud profile and aerosols were observed adjacent to the cloud tops. With concentrations up to 600 cm^{-3} adjacent to cloud tops, the seven cloud profiles from this flight are categorized as "mixing".

An RF was flown on 25 September 2016 (PRF13) during which five vertical cloud profiles and one sawtooth profile were flown (blue, Figure 26). During this flight, the continental low was farther south of the study region and the low RH region at 925mb height was present south of the flight track. A low-pressure system at 925mb, toward the north of the study region, led to high RH along the flight track at the location for the cloud profiles, away from the coast. At these locations, south-southeasterly winds were observed at the surface, with higher geopotential height at 925mb height. Therefore, a deeper boundary layer, with higher cloud tops (890 to 930mb) was sampled. The AOD measured above cloud by 4STAR for the profiles was close to

0.3, except for two profiles including the sawtooth, when high aerosol concentrations were observed adjacent to cloud tops and a higher AOD (0.46) was measured. Aerosol concentrations within 100 m of cloud tops were below 100 cm^{-3} for five of the seven profiles, which were categorized as "separated", and the remaining two, including the sawtooth, were categorized as "mixing".

As shown for PRF05 in Chapter 3, profiles of N_c, R_e and LWC were sampled as a function of altitude, and cloud base and tops were identified for each profile. Variable cloud base and top heights were observed across the forty profiles, due to different sampling locations and variation in environmental conditions at these locations. Therefore, it is difficult to compare the vertical variation in cloud microphysical properties across profiles as a function of altitude. To create a common altitude scale, the vertical variation in cloud properties is examined as a function of normalized height above cloud base, Z_N, (McFarquhar et al. 2007) which is defined as the height above cloud base ($Z - Z_b$) divided by the cloud thickness ($Z_t - Z_b$), where Z_b and Z_t stand for cloud base and top height, respectively, and $Z_t - Z_b$ is the thickness of the cloud.

The derived N_c, R_e and LWC are sorted into ten bins representing Z_N with a constant bin width of 0.1, so that the first bin represents all measurements obtained within Z_N between 0 and 0.1. Further, data from the "mixing" and "separated" cases are plotted separately. The data obtained during "mixing" and "separated" profiles from the six flights are thus examined in a common framework. Figures 27a, 28a, and 29a show box and whisker plots for N_c, R_e and LWC, sampled during the six flights. The center line in each box represents the median, outer edges of the box represent the 25th (Q_1) and 75th (Q_3) percentiles and whiskers extend to $Q_1 - 1.5$ (IQR) and $Q_3 - 1.5$ (IQR), where IQR = $Q_3 - Q_1$, the interquartile range.

For the mixing regime, the median N_c showed little variation with height above cloud base, ranging between 210 to 260 cm^{-3}, with lower values (180 cm^{-3}) near cloud base and top. The median R_e and LWC constantly increased with height, from values of 5.1 μm and 0.05 g m^{-3} near cloud base to 7.2 μm and 0.28 g m^{-3} near cloud top. The IQR for N_c measured over the top half of the cloud deck was 33% greater than the IQR for the bottom half of the clouds, with an average IQR of 320 cm^{-3} for $0.5 < Z_N < 1.0$, and 240 cm^{-3} for $0.0 < Z_N < 0.5$. The greater variability in N_c measured near cloud top is likely associated with the heavy aerosol plume adjacent to cloud tops mixing into the cloud, leading to additional droplet nucleation along with droplet evaporation due to inhomogeneous mixing. This effect extended down to 50% of the cloud deck, suggesting that mixing was affecting cloud properties through at least half of the cloud deck.

For the separated regime, the median N_c ranged between 100 and 150 cm^{-3} with height above cloud base, but decreased to 80 cm^{-3} near cloud top, while the median R_e constantly increased from 6.6 μm near cloud base to 8.8 μm near cloud top. Slightly higher LWC was measured near cloud base, 0.11 g m^{-3} for $0 < Z_N < 0.1$, decreasing to 0.08 g m^{-3} for $0.1 < Z_N < 0.2$ and increasing thereafter with height. The median LWC of 0.25 g m^{-3} for $0.7 < Z_N < 0.8$ decreased closer to cloud top, with median LWC to about 0.2 g m^{-3} for $Z_N > 0.8$. This suggests there was dry air entrainment near cloud tops for "separated" profiles, leading to evaporation of cloud droplets and decreasing the droplet concentration and LWC. A similar decrease in N_c (250 to 180 cm^{-3}) observed near cloud top for the mixing regime suggests dry air entrainment during the mixing profiles.

Near cloud base ($0 < Z_N < 0.1$), fewer and larger cloud droplets were sampled for "separated" profiles, along with greater LWC. The separated regime had a median N_c of about 150 cm^{-3} for 0

27

$< Z_N < 0.1$ while the median N_c measured during "mixing" profiles was about 180 cm^{-3}. In contrast, the median R_e for $0 < Z_N < 0.1$ for the separated regime was 6.6 µm, 28% greater than that measured during the "mixing" profiles, 5.1 µm. The median LWC measured for the separated regime (0.11 g m^{-3}) was also greater than that measured for the mixing regime (0.05 g m^{-3}). It is likely that collision and coalescence of cloud droplets was occurring during these profiles and droplet scavenging near cloud base along with higher R_e resulted in higher LWC despite having lower N_c near cloud base.

Throughout the cloud deck ($0 < Z_N < 1$), the median N_c for the mixing regime was greater than that measured for the separated regime. The difference in the median N_c increased to 130 cm^{-3} for $0.1 < Z_N < 0.2$, and varied between 100 and 150 cm^{-3} throughout the profile. Similarly, the median R_e for the separated regime was greater than the median R_e for the mixing regime for $0 < Z_N < 1$, with a difference of 1.5 to 2 µm. Similar median LWC was observed during the two regimes, with the separated regime having lower LWC for the top 20% of the cloud deck. The median LWC measured during the two regimes was within 0.02 g m^{-3} for $0.1 < Z_N < 0.8$. However, near cloud top, for $0.8 < Z_N < 0.9$ and $0.8 < Z_N < 0.9$, LWC for the mixing regime was greater by 0.07 and 0.09 g m^{-3} respectively, due to the decrease in LWC for the separated regime. Since the "mixing" profiles were observed to have larger droplet concentration with smaller effective radii for $0 < Z_N < 1$, it thus seems that aerosol mixing at cloud tops was affecting cloud properties throughout the cloud deck.

The effects of cloud top mixing on cloud profiles from PRF05 were examined in the previous chapter and inhomogeneous mixing was observed, resulting in a decrease in N_c and LWC near cloud top. A negative correlation between D_v and N_c was observed for some of the profiles as $n(D > 20$ µm$)$ increased resulting from the uptake of water vapor made available by evaporation

28

of smaller droplets (D < 10 μm) near cloud top. A similar decrease in N_c and LWC was observed for both regimes when data for cloud profiles from all six flights were combined (Figures 27 and 29). For the mixing regime, median N_c decreased by 28% from 250 cm^{-3} for 0.8 < Z < 0.9 to 180 cm^{-3} near cloud top (0.9 < Z < 1) and the median N_c for the separated regime decreased by 20%, from 100 cm^{-3} to 80 cm^{-3}. LWC for the separated regime decreased by 20% from 0.25 g m^{-3} to 0.2 g m^{-3} at cloud top while for the mixing regime there was only a slight decrease in LWC from 0.29 to 0.28 g m^{-3}.

Figure 30 shows D_v as a function of N_c, colored by LWC, for the two regimes with measurements made within the top and bottom half of the cloud deck plotted separately. For the bottom half of the clouds, the separated regime had higher D_v with a maximum value of 25.4 μm, compared to 15.5 μm for the mixing regime. Similarly, for the top half, the separated regime had higher D_v with a maximum value of 29 μm, compared to 20.5 μm for the mixing regime. During all four cases, D_v remained constant or increased with decrease in N_c, indicating inhomogeneous mixing throughout the cloud deck during both regimes.

For the separated regime, N_c > 350 cm^{-3} represented less than 5% of the data and for the mixing regime, N_c < 50 cm^{-3} represented less than 2% of the data, and hence these data are outliers. The red lines show mean D_v, averaged over 20 cm^{-3} bins, plotted as a function of N_c. Strictly inhomogeneous mixing was observed for the bottom half of the cloud deck as the slope for the best-fit curve for mean D_v and N_c was -0.0053 for both regimes (the slope remained constant when 0 < N_c < 50 cm^{-3} were included for the separated regime). "Inhomogeneous entrainment mixing with subsequent ascent" was observed for the top half of the cloud deck during the separated regime as a stronger negative D_v-N_c correlation was observed with the best-fit slope decreasing to -0.0193 (changing to -0.0158 when 0 < N_c < 50 cm^{-3} were included). When N_c >

350 cm^{-3} were included in the analysis for the mixing regime, it was observed that strictly inhomogeneous mixing was occurring within both halves of the cloud deck with the best-fit slope for mean D_v and N_c increasing to -.0005 and -0.0017 for the bottom and the top half, respectively. These results suggest that while inhomogeneous mixing was occurring during both regimes, a significant increase in D_v was observed with decrease in N_c for the top half of the cloud deck during separated profiles. This was likely due to the ascent of diluted cloud volumes resulting in an increase in sizes of larger cloud droplets taking up water vapor available from the evaporation of smaller droplets near cloud tops.

While similar meteorological conditions were observed during PRFs 5, 7, 8 and 9, a different meteorological setup was observed during PRFs 11 and 13. As a result, lower cloud tops were sampled during PRF11 with large aerosol concentrations immediately above clouds as all seven profiles from the flight were categorized as "mixing" while higher clouds tops were sampled during PRF13 and only two out of the seven cloud profiles were categorized as "mixing". Therefore, in addition to comparing the vertical change in N_c, R_e and LWC for the two regimes for cloud profiles from all six flights, vertical change in cloud properties for profiles flown during PRFs 5, 7, 8 and 9 (Figures 27b, 28b and 29b) with similar meteorology was also examined.

Figure 27b shows similar higher median N_c (170 cm^{-3}) near cloud base for the mixing regime with the median N_c for the separated regime equal to 150 cm^{-3}. The mixing regime had higher N_c over $0.1 < Z_N < 1$, with the difference varying between 100 and 150 cm^{-3} and a 28% decrease in N_c near cloud top for both regimes. The mixing median R_e increased from 5 µm near cloud base to 7.3 µm near cloud top (Figure 28b) while the separated median R_e increased from 6.7 µm to 8.7 µm and was higher than the median R_e for the mixing regime by 1.5 to 2 µm throughout the

cloud deck. The median LWC for the two regimes was within 0.02 g m^{-3} for 0.1 < Z_N < 0.8. Near cloud base (0 < Z_N < 0.1), the separated regime had higher LWC by 0.07 g m^{-3} while near cloud top, the LWC for the mixing regime was greater by 0.07 and 0.09 g m^{-3}, for 0.8 < Z_N < 0.9 and 0.8 < Z_N < 0.9 respectively, due to the decrease in LWC for the separated regime. Hence, although meteorological conditions affected cloud properties such as cloud thickness and the vertical location of the aerosol and cloud layers, the effect of aerosol mixing at cloud tops on cloud properties remained unaffected by the change in meteorology.

In this study, drizzle droplets are defined as cloud droplets with D>50 µm, and the number concentration of those droplets, hereafter N (D>50 µm), is measured by the 2D-S probe. Similar thresholds have been used in past studies (Wood, 2005a) to separate cloud droplets from drizzle drops. Larger droplets, with greater effective radii, were more frequently observed during cloud profiles with separation between the aerosol plume and cloud tops. This would suggest the collision-coalescence process is occurring more frequently in these cases, which permits the formation of droplet sizes greater than can be produced by condensation alone.

Figures 31 and 32 show the droplet size distributions measured during the fifth profile for sawtooths 1 and 4 (S1e and S4e) respectively, as a function of height. Figures 18, 20 and 21 show the vertical profile for N_c and N_a, R_e and LWC as a function of height for these profiles. While S1e had higher N_c between 200 and 700 cm^{-3} compared with 50 to 100 cm^{-3} for S4e, it had much lower R_e with a maximum value of 6.7 µm, compared with a maximum of 18 µm for S4e. This is consistent with the median D for S1e of 9 µm, and 22.5 µm for S4e. Because of the lack of larger drops needed to initiate the collision-coalescence process, there were few drizzle drops during S1e with no time steps when N (D>50 µm) was greater than 0.1 cm^{-3} during S1e, while for S4e, drizzle concentration was greater than 0.1 cm^{-3} for 30% of the time.

31

Figure 33 shows the probability distribution for the observed concentrations of drizzle drops for the separated and mixing regimes. For the separated regime, the maximum N (D>50 µm) was 2.3 cm^{-3} and the probability of occurrence of N (D>50 µm) > 0.1 cm^{-3} was 0.24. On the other hand, the highest drizzle concentration measured during the mixing regime was 0.9 cm^{-3} with a probability of occurrence of N (D>50 µm) > 0.1 cm^{-3} equal to 0.20. This suggests drizzle concentrations were higher, and had a greater probability of being more than 0.1 cm^{-3} when aerosols were separated from the cloud tops. However, since there is little difference in the probabilities for n(D>50 µm) > 0.1 cm^{-3}, the data needs to be examined for effects of change in parameters such as cloud thickness and vertical velocity that influence drizzle formation.

CHAPTER 5: CONCLUSIONS

In-situ observations of aerosol and cloud properties measured above, within, and below marine stratocumulus over the South-East Atlantic off the coast of Africa during ORACLES 2016 were used to examine how cloud microphysical properties are affected by the change in the vertical location of biomass-burning aerosols relative to cloud tops. Vertical cloud profiles were categorized into two regimes, separated and mixing, based on whether the overlying aerosol plume was separated from or present adjacent to cloud tops and likely mixing into the cloud. The vertical variation in aerosol and cloud properties measured during forty cloud profiles from six research flights were categorized into the two regimes and used to determine the effect of mixing of overlying aerosols into the cloud.

Cloud microphysical properties were measured using cloud probes (i.e., CAS, 2D-S, HVPS and King hot-wire) mounted below the wings of the NASA P-3 aircraft. Aerosol size distributions were measured using the UHSAS ($0.06 < D < 1$ µm) and PCASP ($0.1 < D < 3$ µm) probes aerosol composition was measured using the AMS, and 4STAR was used to retrieve AOD above the aircraft. Artifacts identified in the 2D-S images were rejected using criteria described in Chapter 2, and droplet size distributions n(D), total concentrations N_c, effective radii R_e, and liquid water contents LWC were determined by merging CAS size distributions for $3 < D < 50$ µm and 2D-S size distributions for $50 < D < 1280$ µm. Throughout this study, thresholds of LWC > 0.05 g m^{-3} and $N_c > 10$ cm^{-3} were used to define a cloud. Mass closure tests revealed that the bulk LWC measured by the King hot-wire was strongly correlated (R=0.77) with LWC calculated by integrating the droplet mass distribution for $12.5 < D < 40$ µm. The LWC calculated from the SDs overestimated the bulk LWC up to 30% of the time when smaller

droplets (3 < D < 12.5 µm) were included likely due to the hot-wire's decreased collision efficiency for smaller droplets. Hence, the LWC calculated from the SDs was used in this study to characterize the mass content of the clouds.

A case study examined eight cloud profiles flown on 6 September 2016 (PRF05). Although inter-comparison with another PCASP used on the BAe146 during ORACLES 2017 and with the UHSAS over the same size range during ORACLES 2016 suggested that the UND PCASP n(D) was biased low, especially for D < 300 nm, the UND PCASP N_a could still be used to identify the location of the aerosol plume. HYSPLIT back trajectories determined the aerosol source region and explained the variation in above and below-cloud aerosol mass concentration and composition between profiles. Aerosol composition observed above cloud tops was indicative of biomass-burning products and differed from the composition below clouds, which did not show evidence of biomass-burning aerosols.

Flight modules flown during PRF05 were designed to sample clouds and aerosols in-situ above, within and below cloud and included four sawtooth profiles and four individual vertical profiles. Sawtooth profiles comprised of multiple cloud profiles where each profile lasted for 90 to 150 seconds, covering a horizontal distance between 10 and 17 km. The AOD measured above the P-3 immediately before or after the sawtooths averaged above 0.4, suggesting a heavy aerosol plume was present above the cloud deck during each sawtooth. During sawtooth 4 (S4), low N_a (<20 cm^{-3}) was sampled immediately above cloud tops and enhanced N_a (> 100 cm^{-3}) was separated from the cloud deck by about 200 m. Consequently, this profile was categorized into the "separated" regime, which included cloud profiles with the aerosol plume (N_a > 100 cm^{-3}) separated from cloud tops by at least 100 m. During S1, S2 and S3, high aerosol concentrations up to 600 cm^{-3} were observed adjacent to cloud tops. These aerosols were likely mixing into the

cloud and these profiles were categorized into the "mixing" regime, which included cloud profiles with $N_a > 100$ cm^{-3} within 100 m of cloud tops.

A similar methodology was used to categorize each sawtooth and profile flown during ORACLES 2016 as separated or mixing. A statistical analysis was conducted using data from six research flights, PRFs 5, 7, 8, 9, 11 and 13 flown on 6, 10, 12, 14, 20 and 25 September 2016 respectively, when at least 1000 s were spent in cloud and at least three cloud profiles were flown. Forty cloud profiles, flown between 10° S to 20° S and 0° to 12° E, were categorized into the two regimes and twenty-four separated and sixteen mixing profiles were identified. Only two profiles had AOD below 0.25, suggesting the aerosol plume was present above the cloud deck during all other profiles, regardless of its vertical location or separation from the cloud deck.

The effect of aerosol mixing at cloud tops was observed throughout the cloud deck as more numerous and smaller cloud droplets were observed during the mixing profiles. The median N_c ranged between 180 to 260 cm^{-3} for the mixing regime and the IQR for N_c measured over the top half was 33% greater than that for the bottom half due to activation of aerosols mixing into cloud tops. In comparison, the median N_c for the separated regime was lower by 100 to 150 cm^{-3} for $0.1 < Z_N < 1$ indicating that the mixing at cloud tops affected droplet concentrations down to cloud base. In addition, the separated regime had median R_e between 6.6 to 8.8 µm which was greater than that for the mixing regime by 1.5 to 2 µm throughout the cloud. The median LWC for the two regimes was within 0.02 g m^{-3} for $0.1 < Z_N < 0.8$ with the separated regime having higher LWC near cloud base due to the presence of large droplets falling out of cloud, and lower LWC near cloud top due to dry air entrainment.

It was observed that the median N_c and LWC decreased near cloud tops during both regimes. This was due to inhomogeneous mixing throughout the cloud deck as similar mean volume

diameters, D_v were measured with decreasing N_c within the top and the bottom half of the cloud. In the separated regime, the mixing of dry air into cloud tops led to the evaporation of smaller droplets and the water vapor made available by the droplet evaporation was taken up by larger droplets which grew in size. Consequently, a negative correlation was observed between D_v and N_c for the top half of the cloud since D_v increased as N_c decreased. In contrast, in the mixing regime, aerosols were likely mixing into the cloud along with the sub-saturated air. Competition for water vapor between the larger droplets and newly activated aerosols led to little change in D_v as N_c decreased.

More numerous but smaller cloud droplets were observed when aerosols were mixing into cloud tops. Consequently, precipitation was suppressed during the mixing regime as a higher probability of drizzle occurrence was observed for the separated regime. Higher concentrations of drizzle were also observed for the separated regime. However, constraining parameters such as cloud thickness and vertical velocity is required to further examine the effect of cloud-top mixing of aerosols on the onset of collision-coalescence and formation of precipitating droplets.

The differences between cloud microphysical properties measured during the two regimes remained consistent when only data for cloud profiles from four flights with similar meteorology were compared and when data from two more flights, with different meteorology, were included. Therefore, even though environmental conditions affect cloud properties such as thickness, top height, and vertical location of the aerosol plume relative to cloud, the effects of aerosol mixing into cloud tops remains the same.

Flight Date	Time in Cloud	Sawtooths	Vertical Cloud profiles
PRF05: September 06	4084 s	4	4
PRF07: September 10	2417 s	1	7
PRF08: September 12	1374 s	1	2
PRF09: September 14	2879 s	0	8
PRF11: September 20	1876 s	1	6
PRF13: September 25	1838 s	1	5
Total	4h 1m 8s	8	32

Table 1: Research flights used in the study, including time in cloud, number of sawtooths performed and number of ascents/descents along a constant heading (vertical cloud profiles).

Flight Date	Correlation Coefficient LWC for D > 3 µm (LWC for 12.5<D<40)	Best-fit slope LWC for D > 3 µm (LWC for 12.5<D<40)	LWC_{CAS}/LWC_{KING} LWC for D > 3 µm (LWC for 12.5<D<40)
September 06	0.590 (0.609)	0.844 (0.594)	0.958 (0.488)
September 10	0.761 (0.835)	0.728 (0.756)	0.722 (0.527)
September 12	0.833 (0.890)	0.603 (0.598)	0.560 (0.372)
September 14	0.452 (0.747)	0.460 (0.591)	0.723 (0.331)
September 20	0.629 (0.717)	0.809 (0.736)	1.044 (0.543)
September 25	0.747 (0.813)	0.553 (0.630)	0.848 (0.508)

Table 2: R, best-fit slope and LWC ratio for CAS LWC integrated over 3 < D < 50 µm and 12.5 < D < 40 µm.

Sawtooth	Time (UTC)	Latitude (°S)	Longitude (°E)	AOD	COT	COT (Aqua)
09/06–S1	08.46 – 08.56	19.77 – 19.00	Along 9E	0.41	29.2	-
09/06-S2	10.11 – 10.21	13.30 – 12.54	Along 9E	0.39	14.7	5 – 18
09/06-S3	11.07 – 11.19	10.02 – 10.79	Along 9E	0.52	17.5	3 – 17
09/06-S4	13.15 – 13.26	18.91 – 19.57	11.6 – 11.9	0.41	8.31	5 – 10
09/06-P1	09.02 – 09.03	18.56 – 18.51	Along 9E	0.14	10.9	6 – 8
09/06-P2	09.36 – 98.38	15.94 – 15.85	Along 9E	0.28	43.2	6 – 12
09/06-P3	12.34 – 12.35	16.33 – 16.39	10.7 – 10.73	0.44	8.90	6 – 10
09/06-P4	11.33 – 11.34	11.73 – 11.80	9.08 – 9.11	0.27	14.4	15 – 20

Table 3a: Parameters listed for cloud profiles flown on PRF05.

Sawtooth	Regime	ΔZ (m)	LWP (gm^{-2})	Pressure (mb)	Temperature (C)
09/06–S1	Mixing	276	118.9	910 – 960	9.0 – 19.2
09/06-S2	Mixing	330	60.36	915 – 960	12.5 – 22.2
09/06-S3	Mixing	484	81.54	904 – 969	13.0 – 17.5
09/06-S4	Separated	245	51.87	956 – 994	11.2 – 14.0
09/06-P1	Separated	177	36.12	926 – 948	10.2 – 11.8
09/06-P2	Mixing	334	181.2	920 – 959	10.5 – 20.2
09/06-P3	Mixing	290	33.39	943 – 979	12.5 – 16.0
09/06-P4	Mixing	328	57.24	914 – 952	12.8 – 15.5

Table 3b: Parameters listed for cloud profiles flown on PRF05.

Flight Date	Type	Cloud time	Sawtooths	Individual profiles	Mixing	Separated
PRF05: September 06	TF	4084 s	4	4	6	2
PRF07: September 10	RF	2417 s	1	7	0	8
PRF08: September 12	RF	1374 s	1	2	1	2
PRF09: September 14	TF	2879 s	0	8	0	8
PRF11: September 20	TF	1876 s	1	6	7	0
PRF13: September 25	RF	1838 s	1	5	2	4
Total		**4h 1m 8s**	**8**	**32**	**16**	**24**

Table 4: Research flights used in this study based on cloud time and number of cloud profiles flown.

Figure 1: (A) CDP (B) King hot-wire (C) 2D-S and (D) HVPS3 mounted under the right wing of NASA P-3.
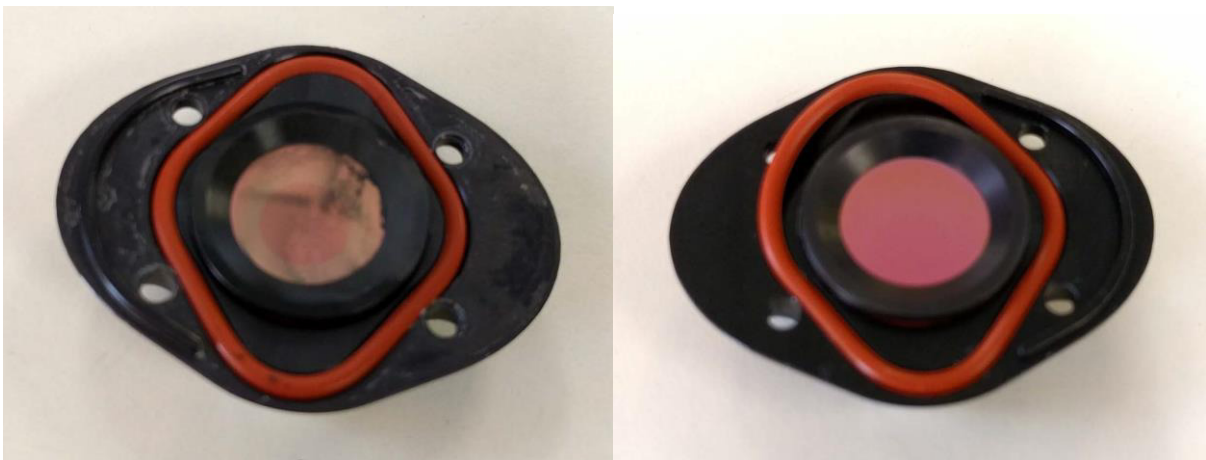
Figure 2: Aerosol deposition on the inside of the receive side mirror for the 2D-S vertical channel, cleaned mirror on the right.
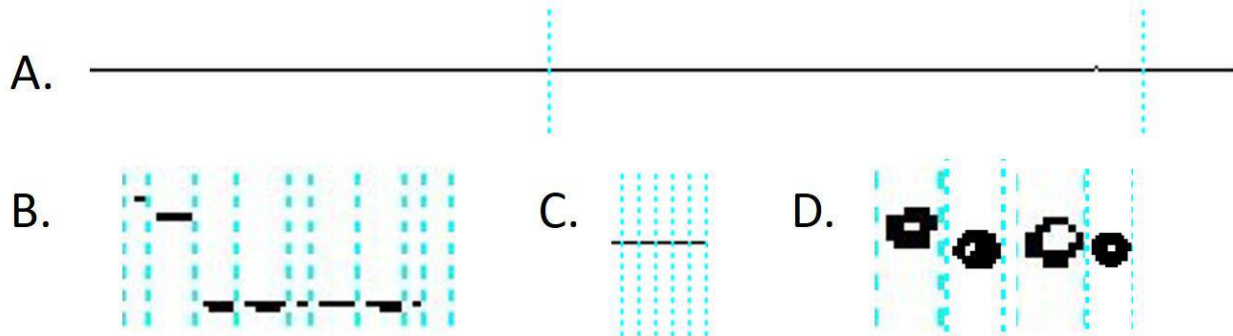
Figure 3: 2DS images of (a) a continuously stuck diode, (b) multiple stuck diodes, (c) an intermittently stuck diode, and (d) out-of-focus droplets. The dashed blue lines separate individual particles.
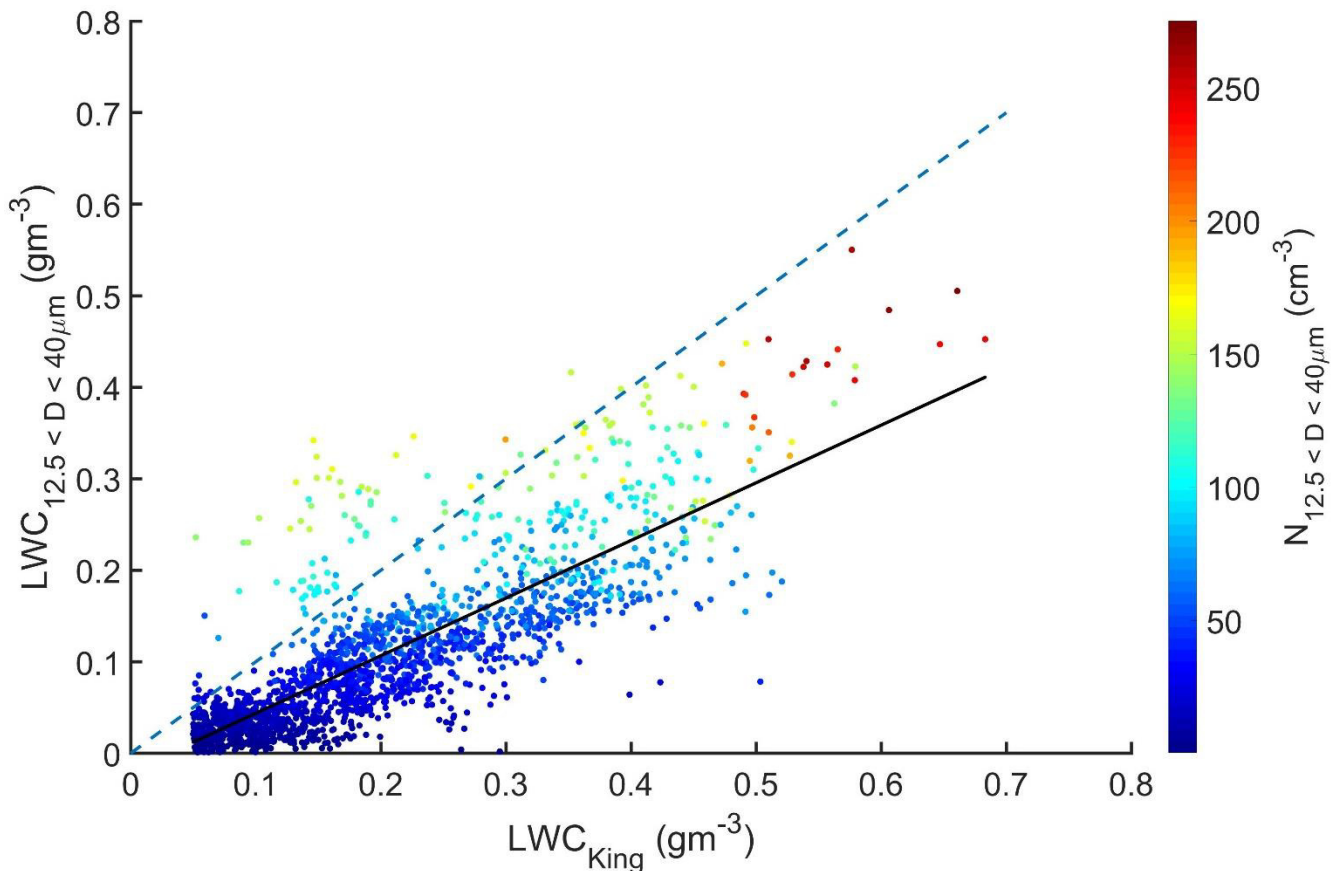
Figure 4: Scatter between King LWC and the LWC derived by integration of droplet mass distribution for 12.5 < D < 40 µm from PRF13 (25 September 2016), colored by N (12.5 < D < 40 µm).
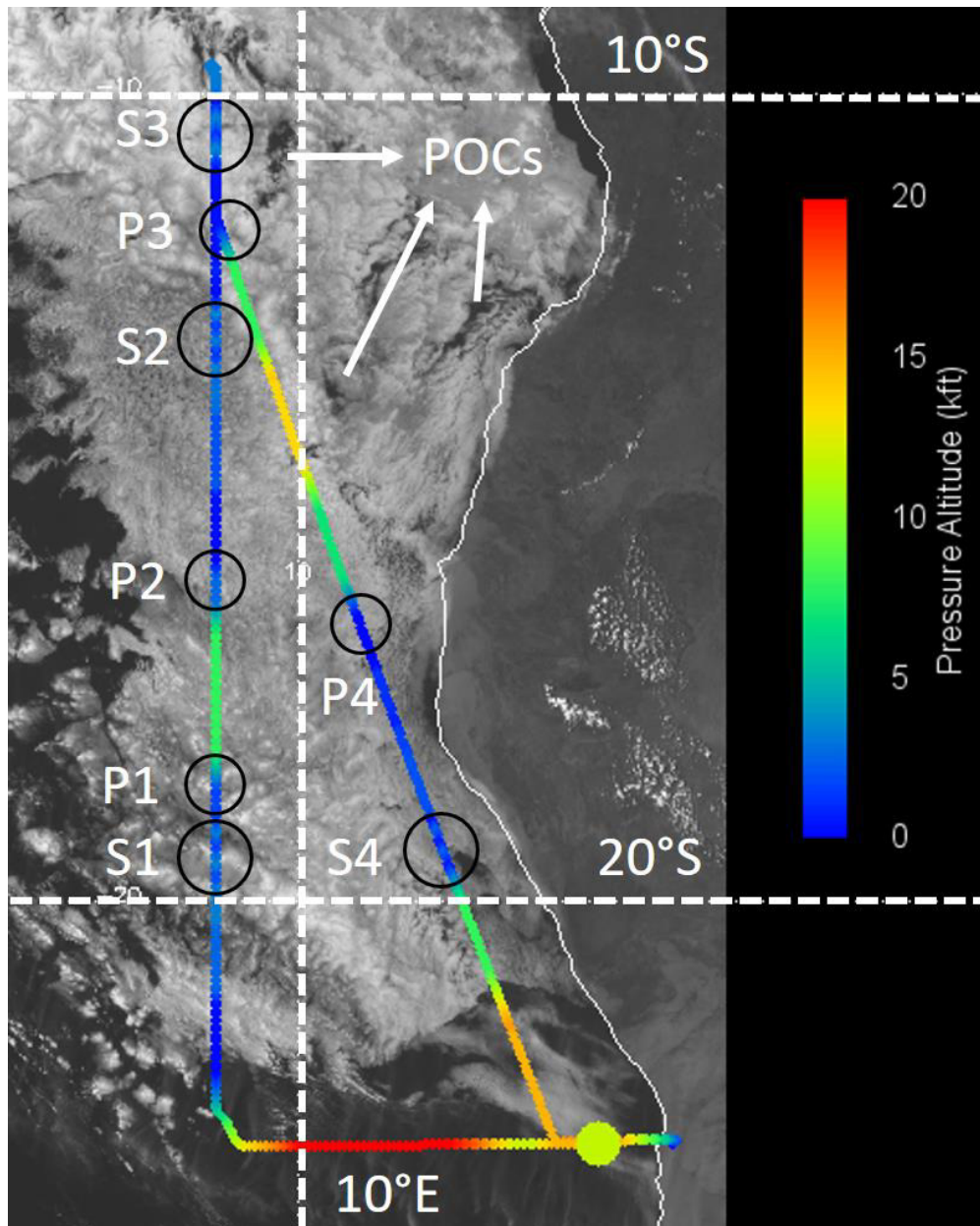
Figure 5: Spinning Enhanced Visible and Infrared Imager, SEVIRI visible image at 14.00 UTC on 6 September 2016 (PRF05), overlaid by the PRF05 flight track, and colored by flight altitude. Circles indicate sawtooth (S) and vertical profile (P) locations.
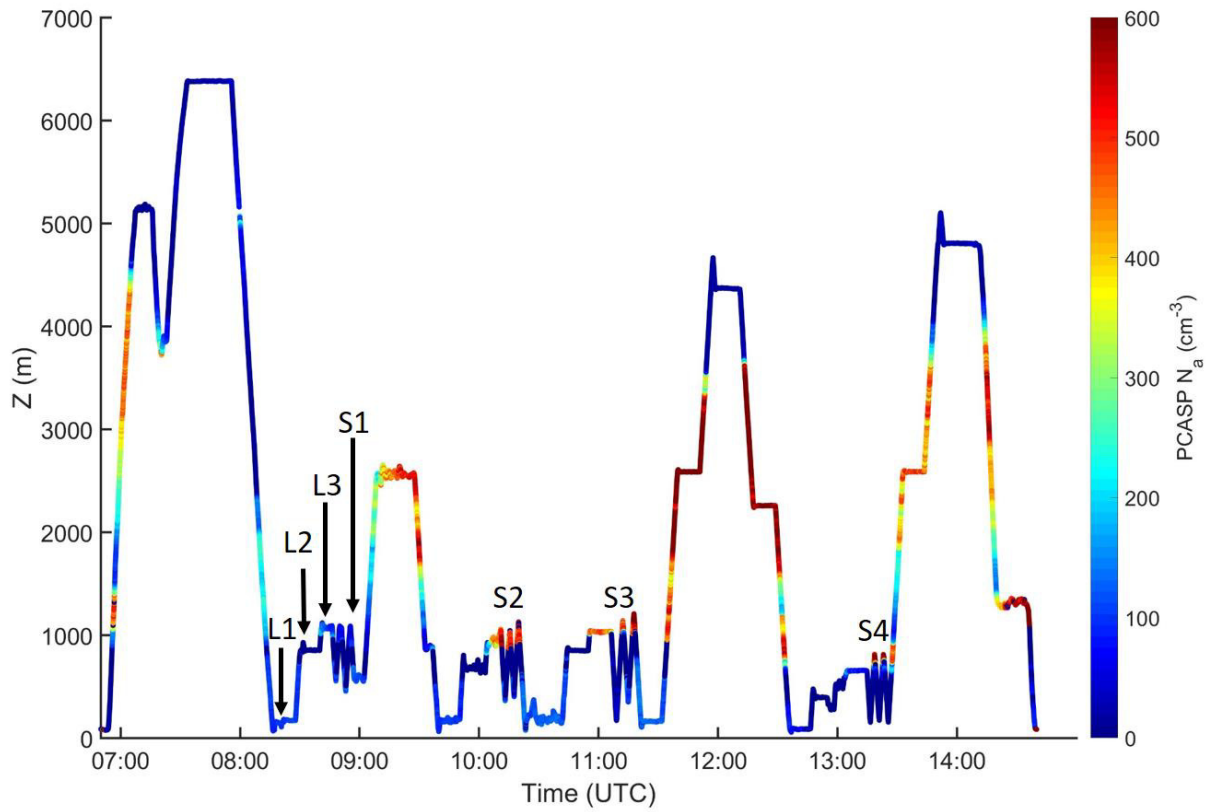
Figure 6: Altitude flown by the P-3 as a function of time for 6 September 2016 (PRF05), colored by PCASP N_a.
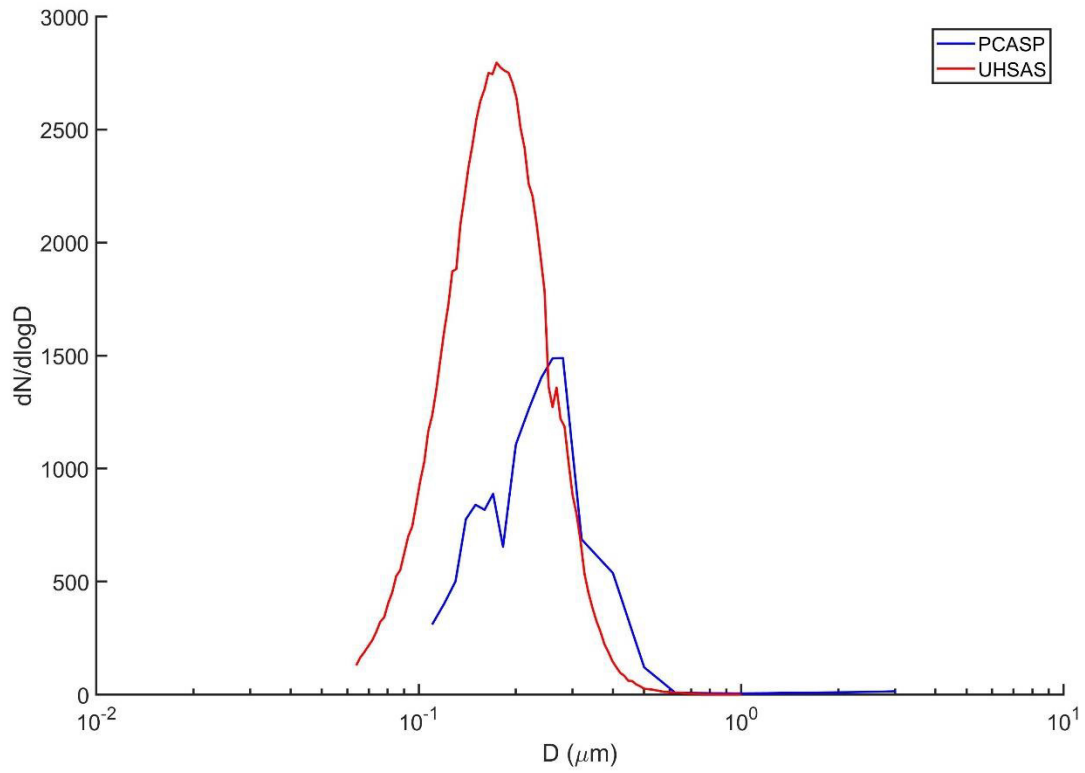
Figure 7: Mean aerosol size distribution measured by the PCASP and UHSAS from PRF05 at altitudes between 2000 m and 3000 m.
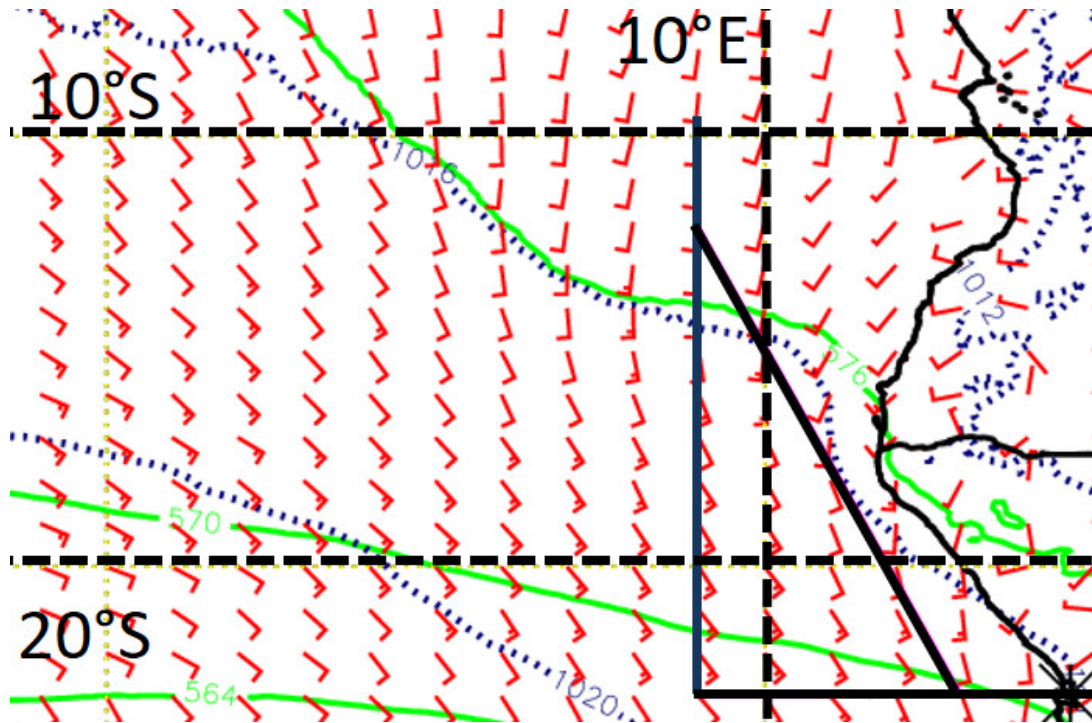
Figure 8: 0-hour forecast at 12.00 UTC on 6 September 2016 (PRF05) from the European Centre for Medium-Range Weather Forecasts, ECMWF for mean sea level pressure (dashed blue), 500mb geopotential height (solid green) and surface winds, overlaid by the PRF05 flight track.
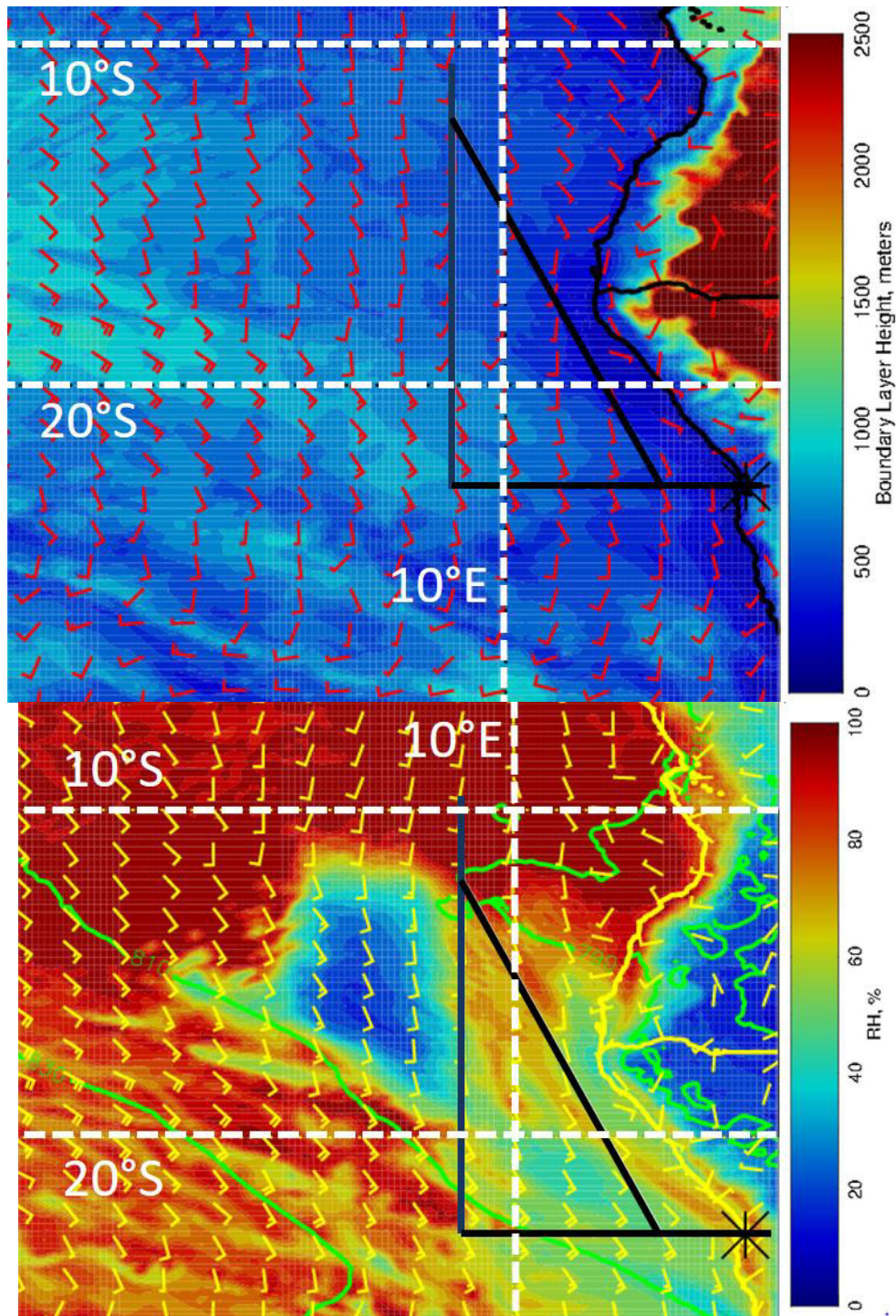
Figure 9: 0-hour forecast at 12.00 UTC on 6 September 2016 (PRF05) from ECMWF for boundary layer height and 900 mb wind (top) and 925mb relative humidity (colored), geopotential height (solid green) and wind, overlaid by the PRF05 (6 September 2016) flight track.
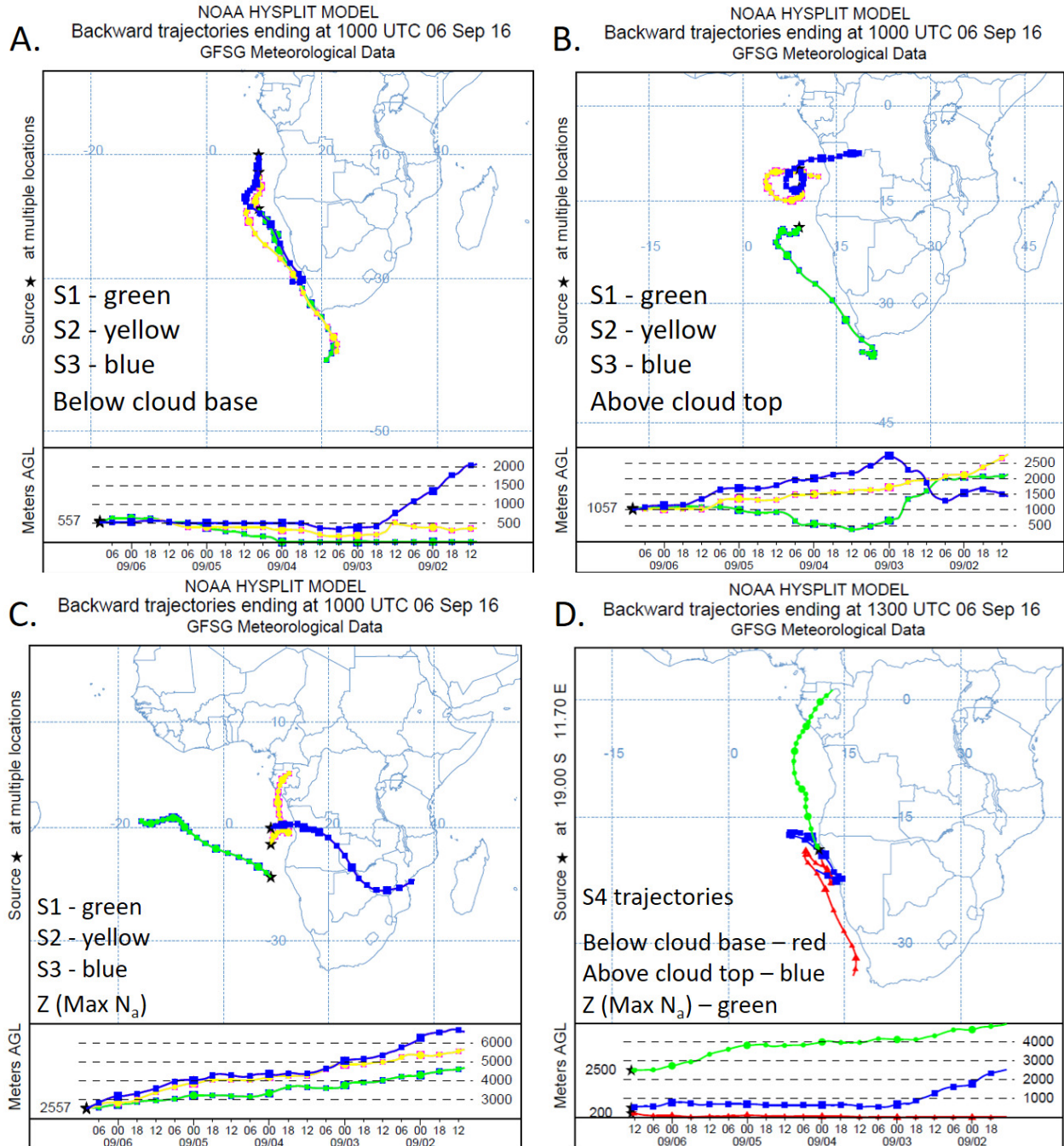
Figure 10: 5-day back-trajectories from the NOAA HYSPLIT model for PRF05 (6 September 2016). (A) ending at 10.00 UTC for S1 - S3 near cloud base (500 m) (B) ending at 10.00 UTC for S1 - S3 near cloud top (1000 m) (C) ending at 10.00 UTC for S1 – S3 near maximum PCASP N_a (2500 m) and, (D) ending at 13.00 UTC for S4 near cloud base, cloud top and maximum PCASP N_a (200 m, 500 m and 2500 m). Altitudes shown represent values above mean sea level.
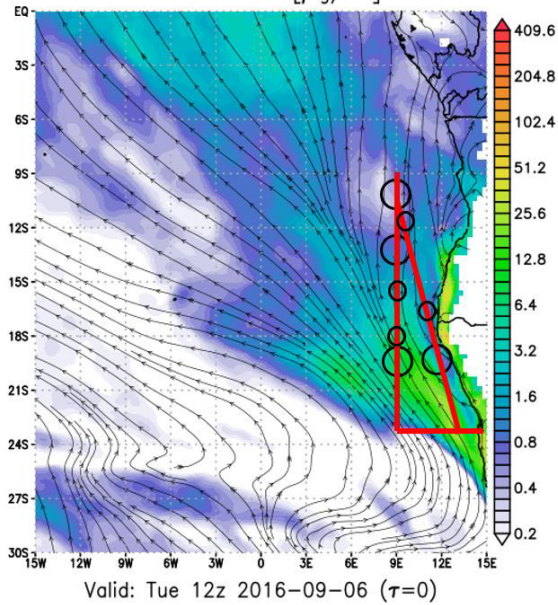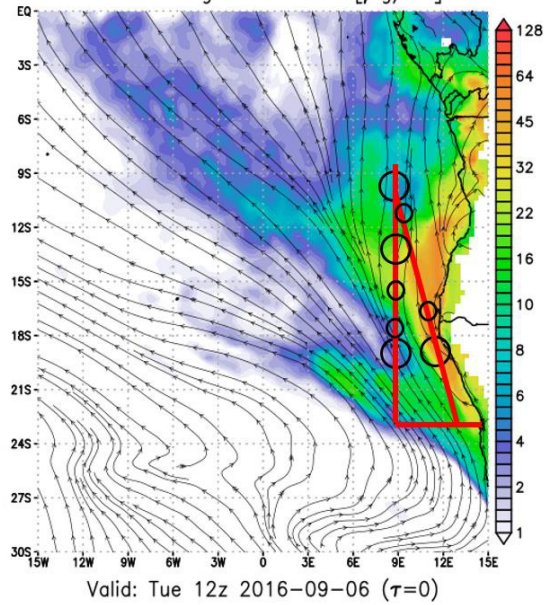
Figure 11: The Goddard Earth Observing System Model Version-5, GEOS-5 forecasts for dust and organic carbon at 925mb height valid at 12.00 UTC on 6 September 2016 (PRF05), overlaid by the PRF05 flight track with circles indicating profile locations.
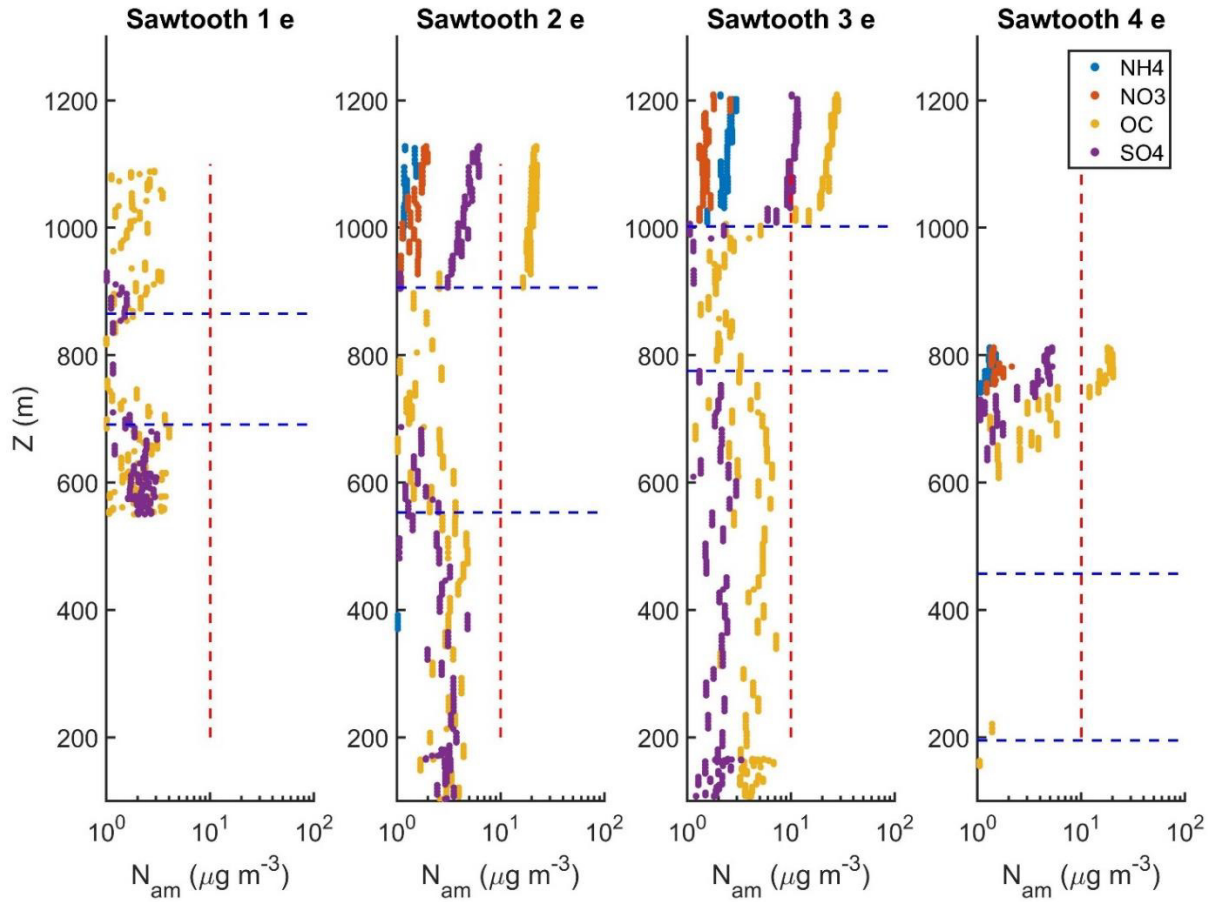
Figure 12: Aerosol mass concentration, N_{am} as a function of Z for the fifth profile flown during sawtooth legs on PRF05 (6 September 2016), colored by aerosol type. The dashed blue lines represent cloud base and top, the dashed red line represents 10 µg m^{-3}.
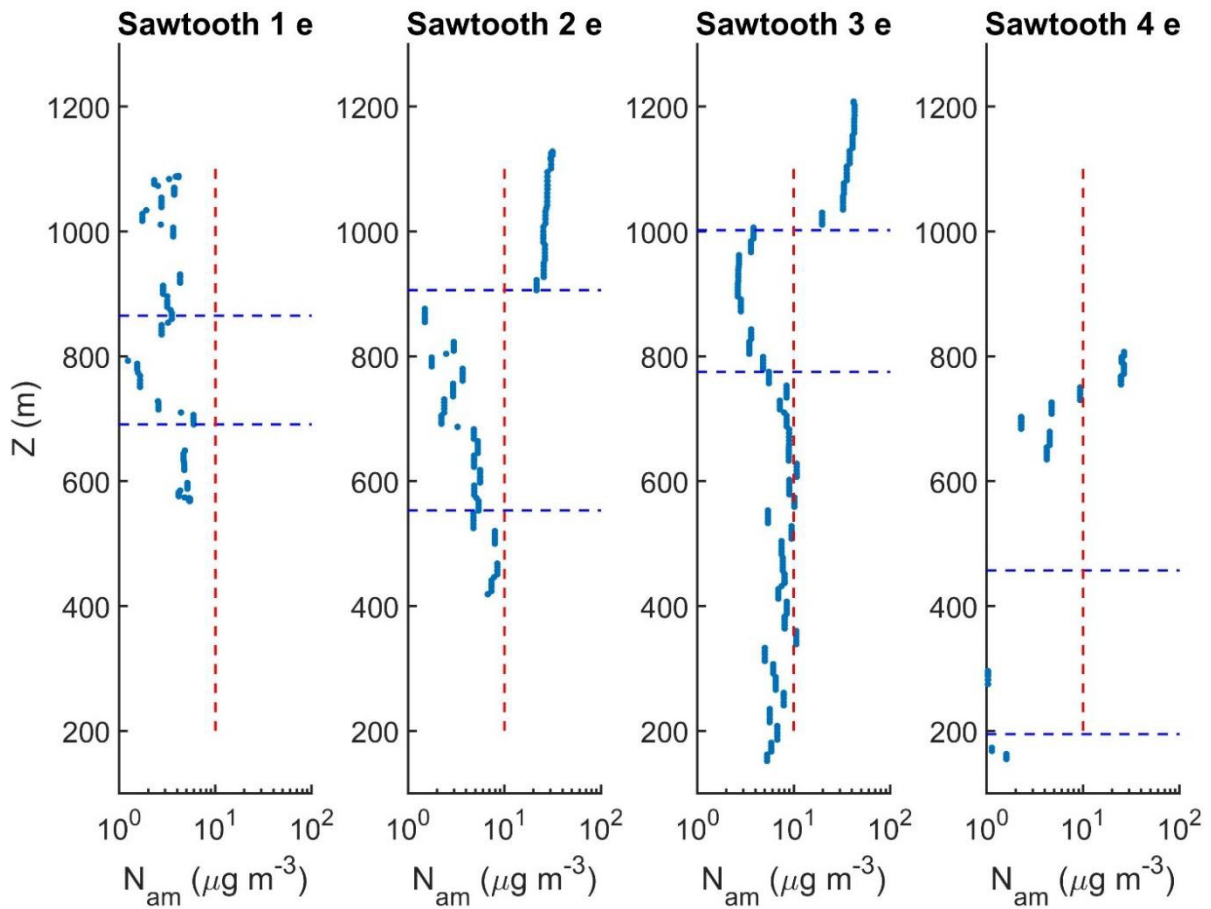
Figure 13: Total aerosol mass concentration, N_{am} measured by the AMS as a function of Z for the fifth profile flown during sawtooth legs on PRF05 (6 September 2016). The dashed blue lines represent cloud base and top, the dashed red line represents $10 \, \mu g \, m^{-3}$.
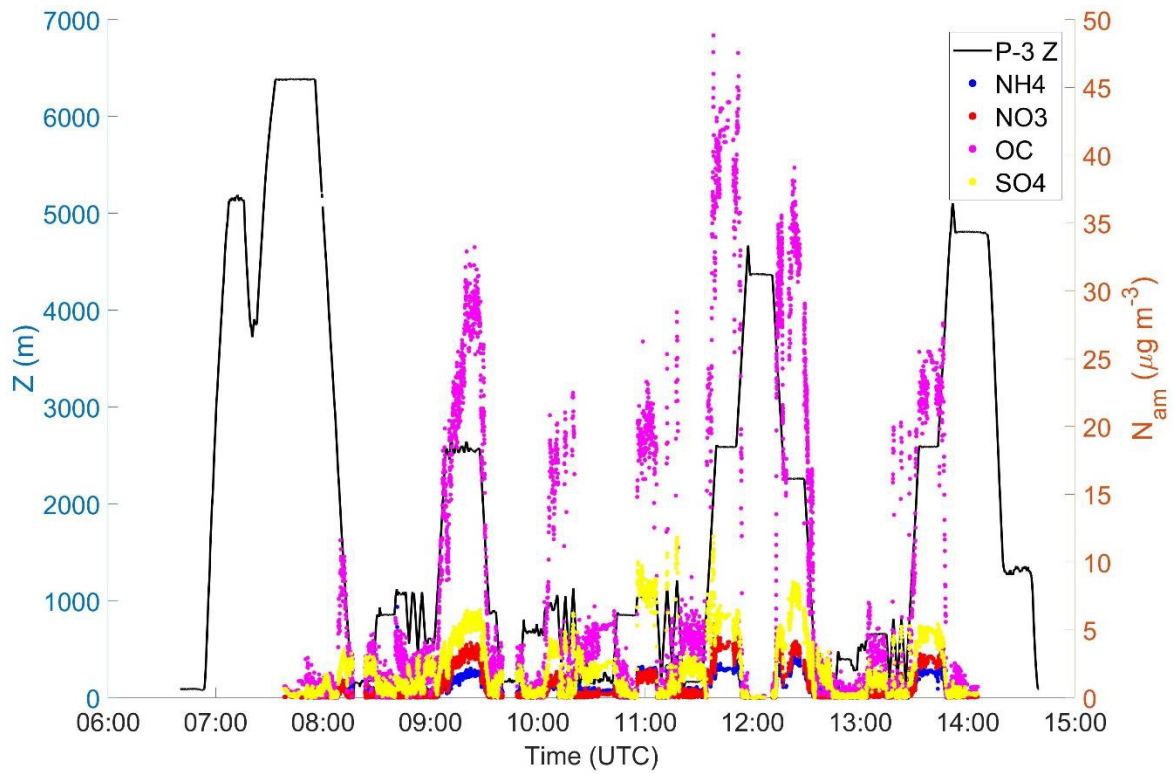
Figure 14: Altitude flown by the P-3 from PRF05 (6 September 2016), overlaid by the aerosol concentration measured by the AMS, colored by aerosol type, as shown in legend.
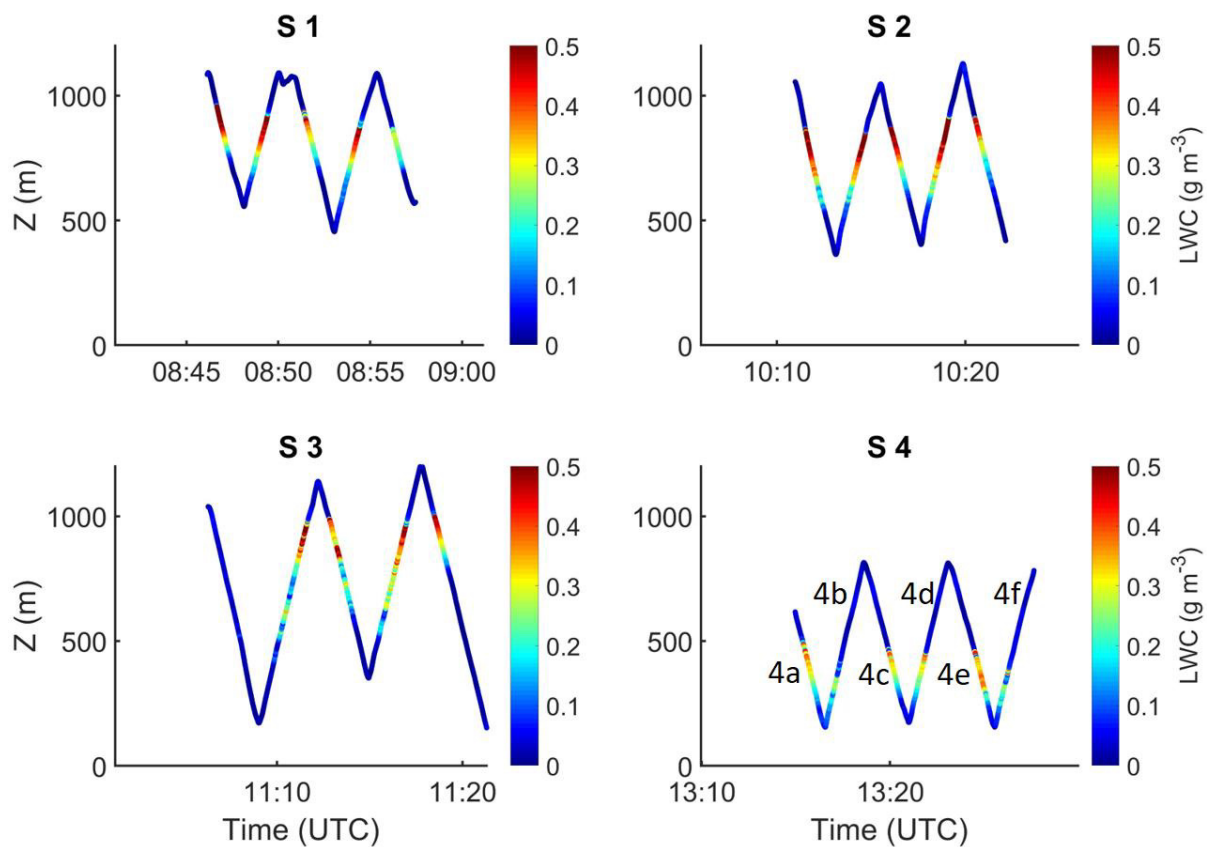
Figure 15: The NASA P-3 altitude as a function of time during sawtooth profiles from PRF05 (6 September 2016), colored by King LWC.
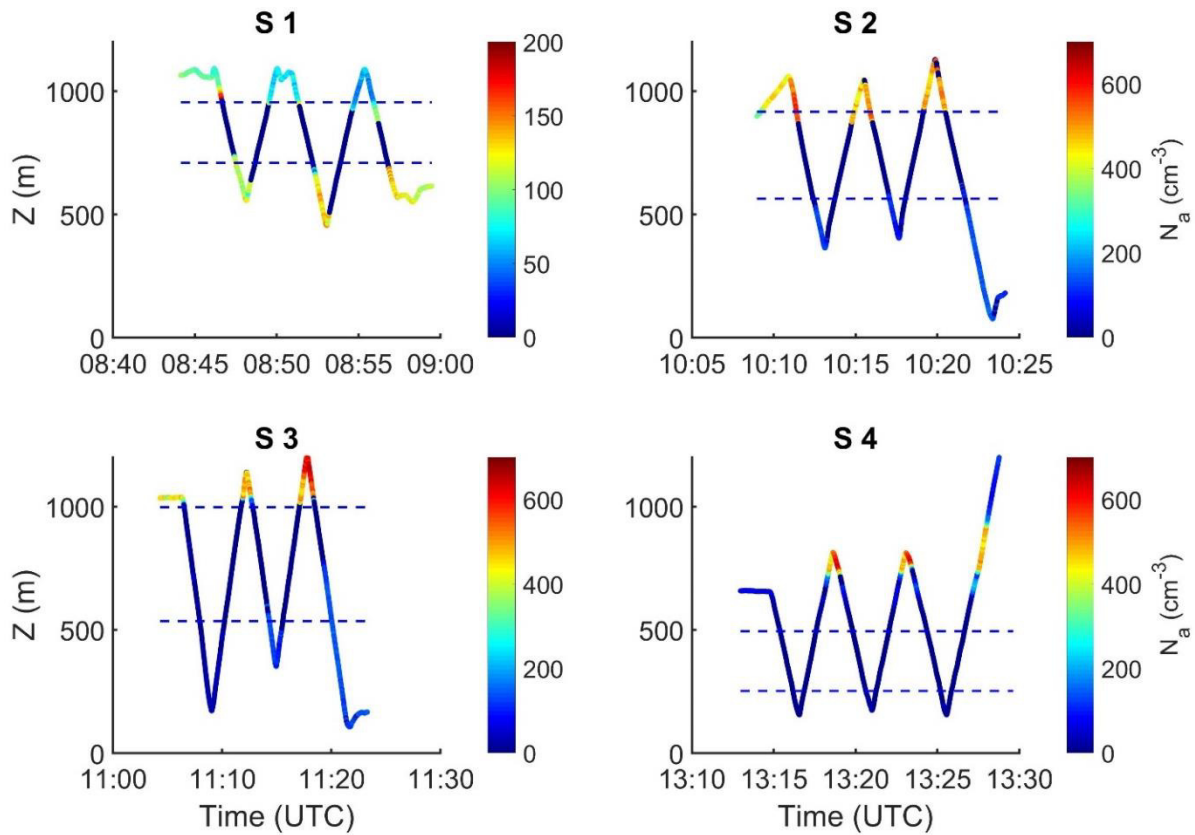
Figure 16: The NASA P-3 altitude as a function of time during sawtooth profiles (two minutes before and after the profile included) from PRF05 (6 September 2016), colored by the accumulation-mode aerosol concentration, N_a measured by the PCASP. Dashed blue lines mark the approximate cloud base and top.
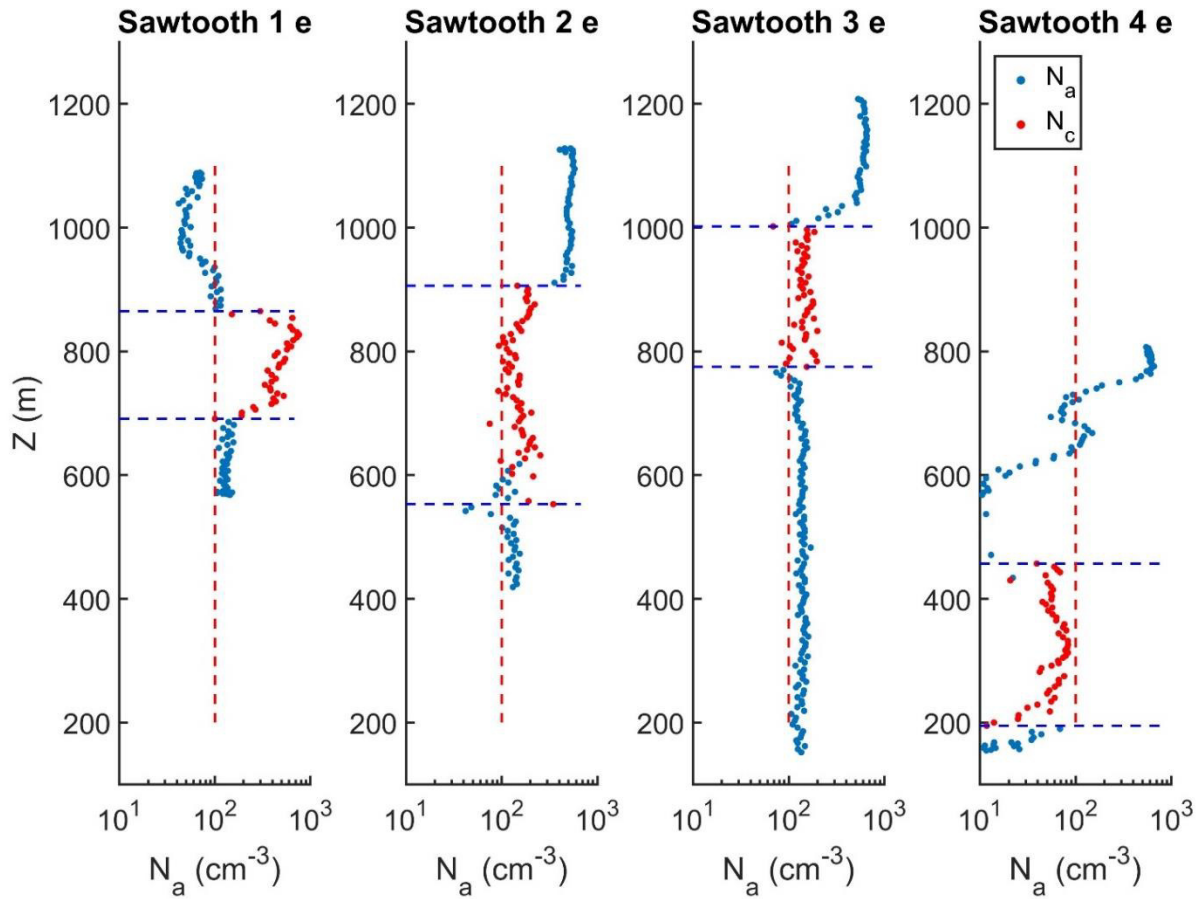
Figure 17: N_c and PCASP N_a as a function of Z for the fifth profile flown during the sawtooth legs on PRF05 (6 September 2016). Dashed blue lines represent cloud base and top for the profile, the dashed red line marks 100 cm^{-3}.
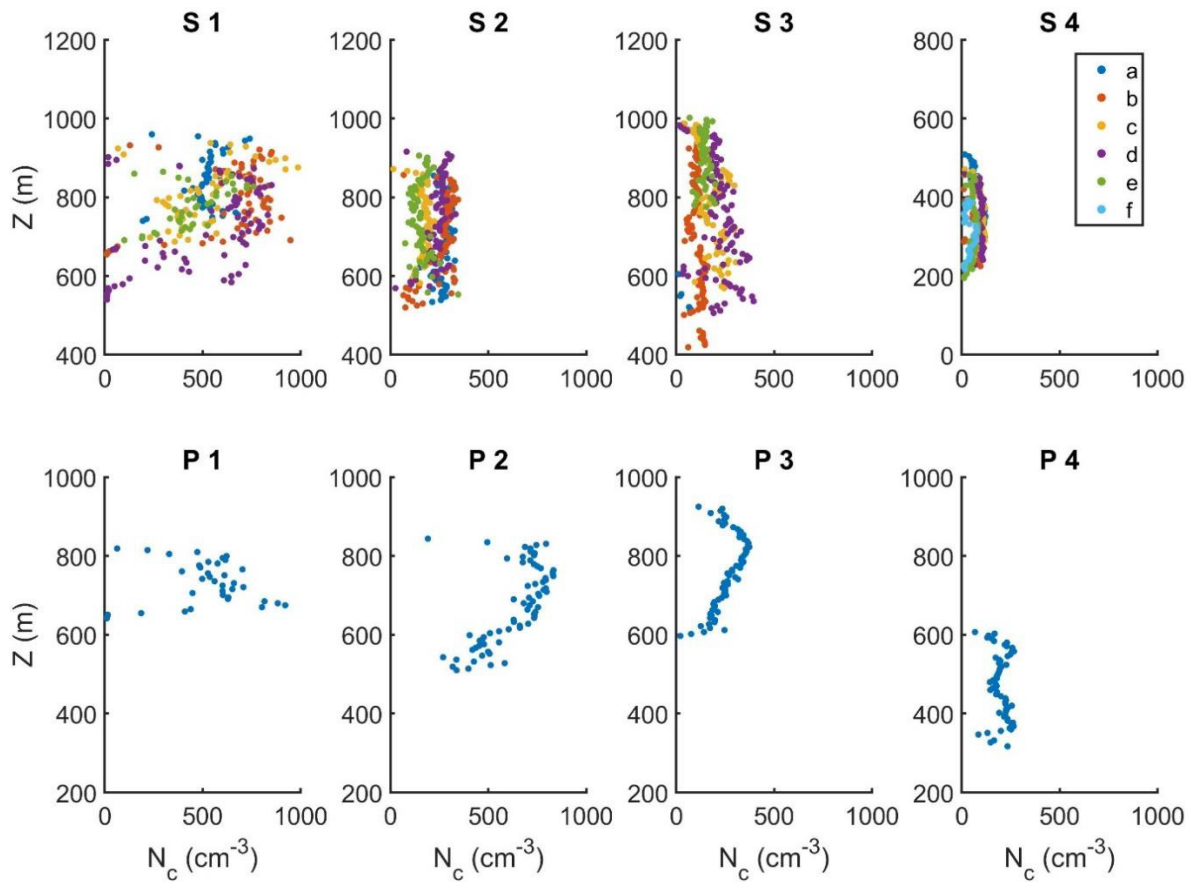
Figure 18: N_c as a function of Z, for four sawtooth legs colored by individual profiles (top) and individual profiles (bottom), from PRF05 (6 September 2016).
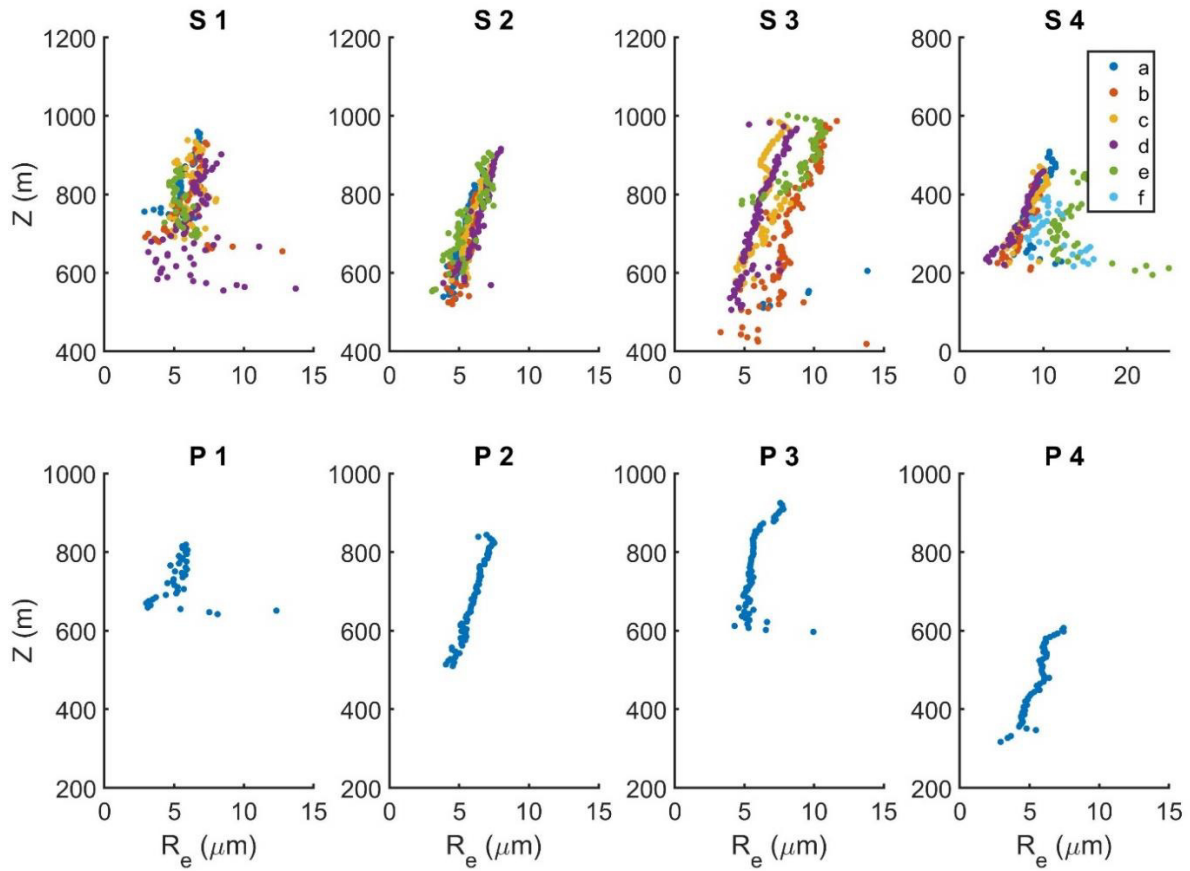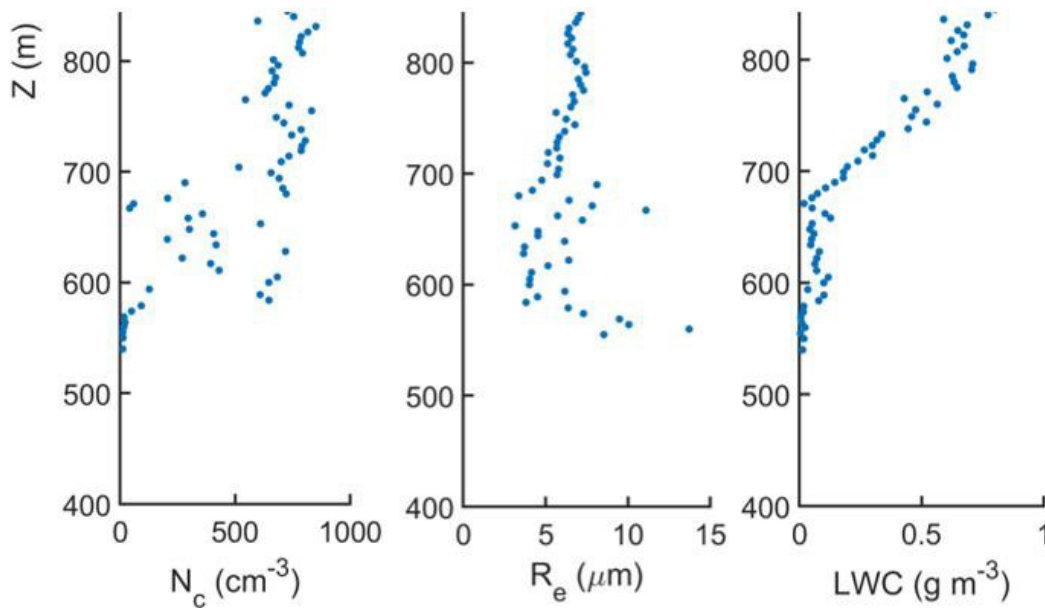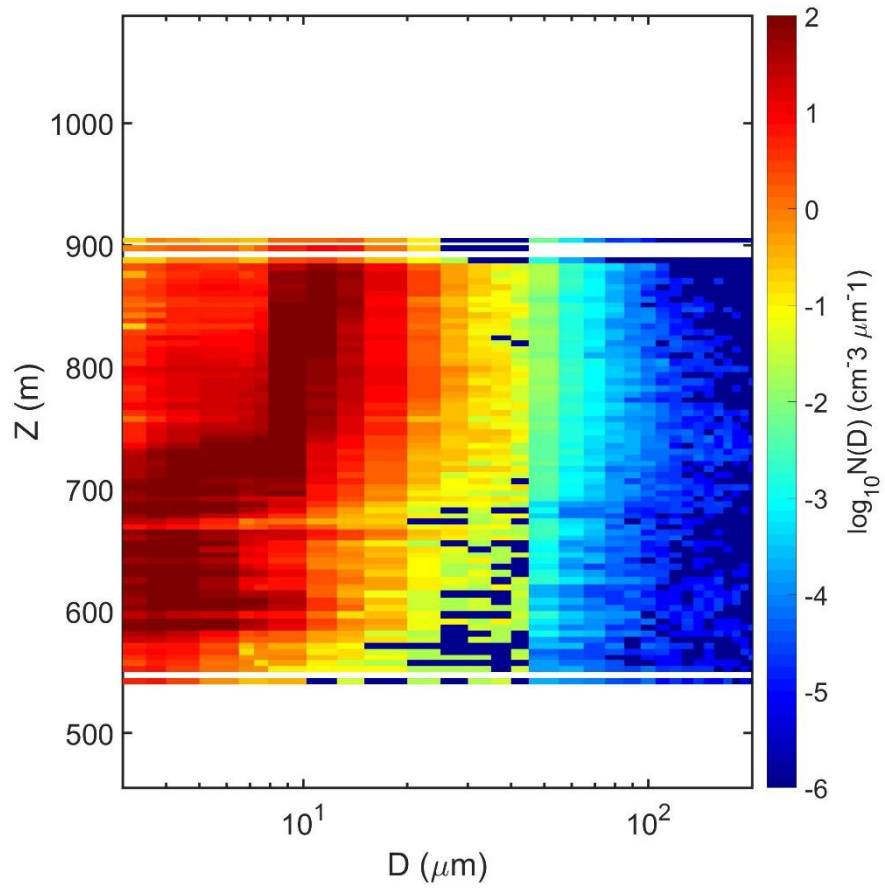
Figure 19: R_e as a function of Z, for four sawtooth legs colored by individual profiles (top) and individual profiles (bottom), from PRF05 (6 September 2016).
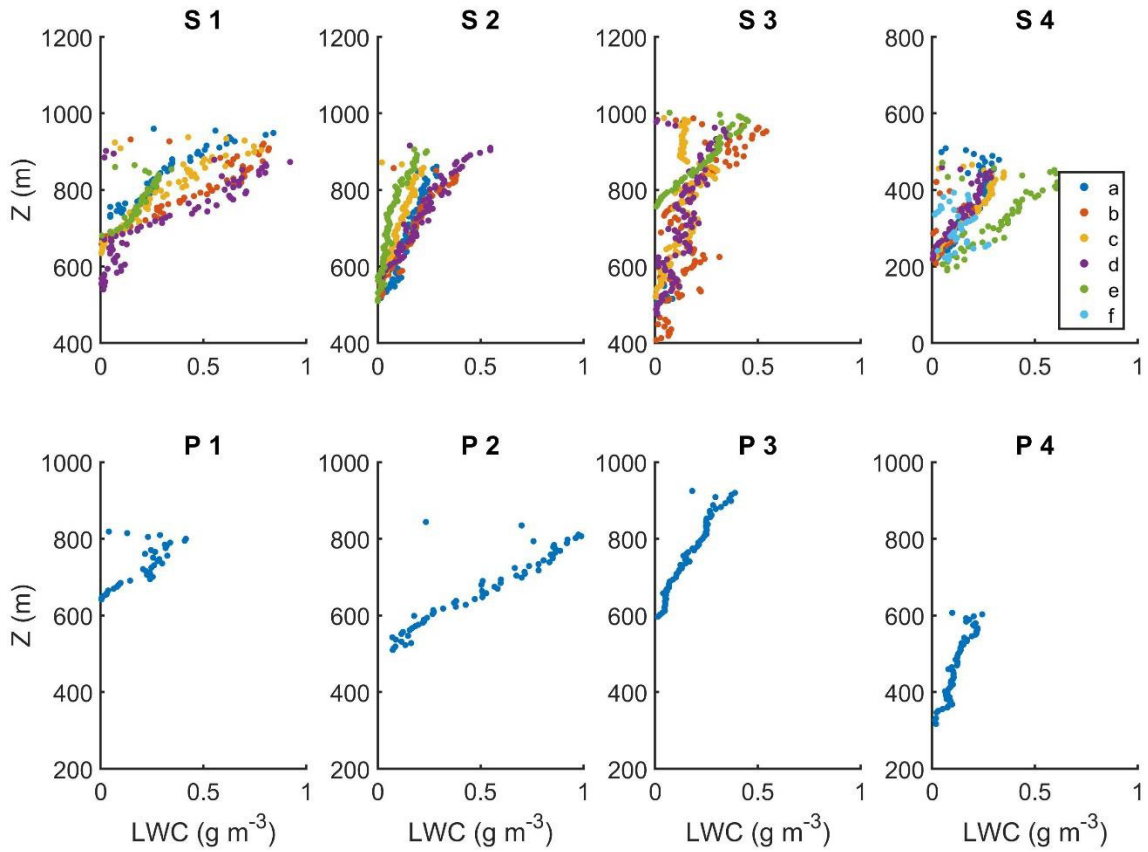
Figure 20: LWC as a function of Z, for four sawtooth legs colored by individual profiles (top) and individual profiles (bottom), from PRF05 (6 September 2016).

Figure 21: N_c, R_e, and LWC as a function of Z during S1d from PRF05.

Figure 22: Droplet size distribution for 3 < D < 500 µm as a function of Z for S1d from PRF05, colored by the logarithm of the number distribution function for each size bin.
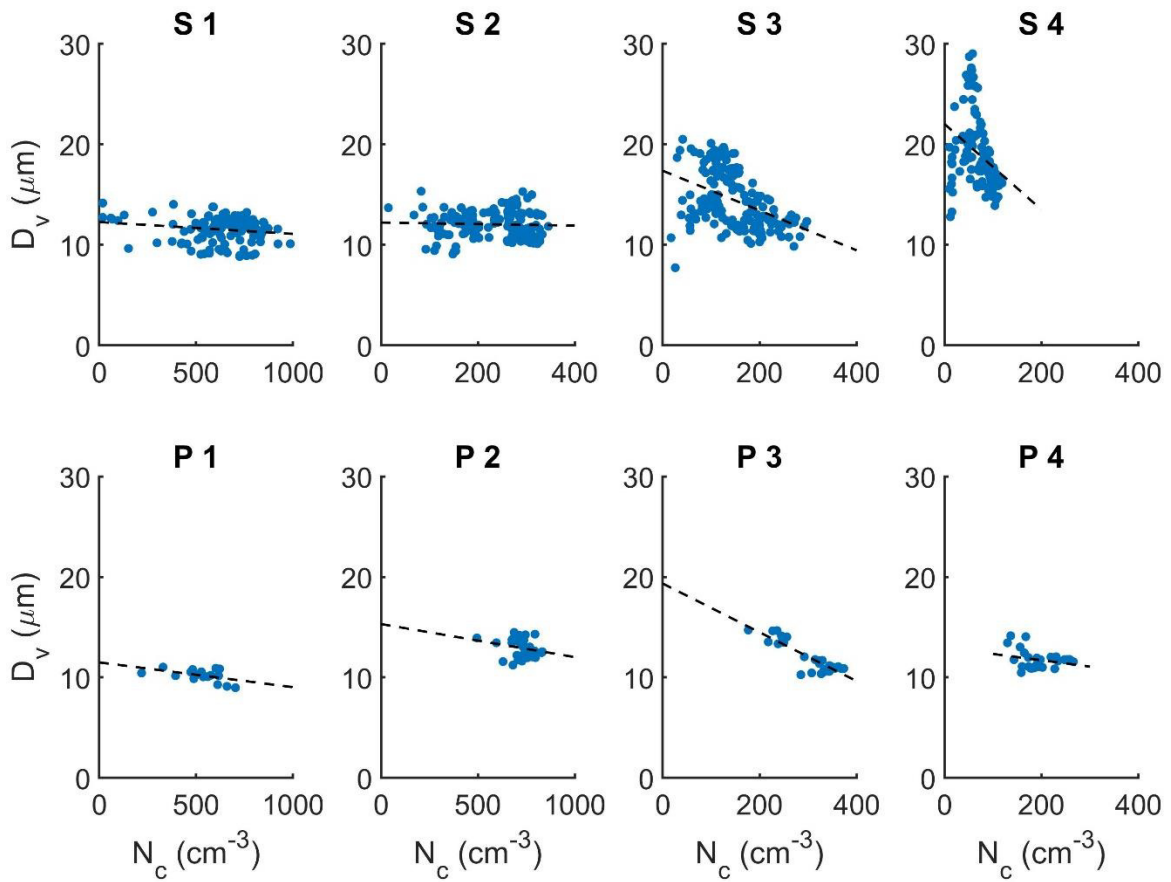
Figure 23: Mean volume diameter (D_v) plotted as a function of N_c for the sawtooth legs and individual profiles from PRF05.
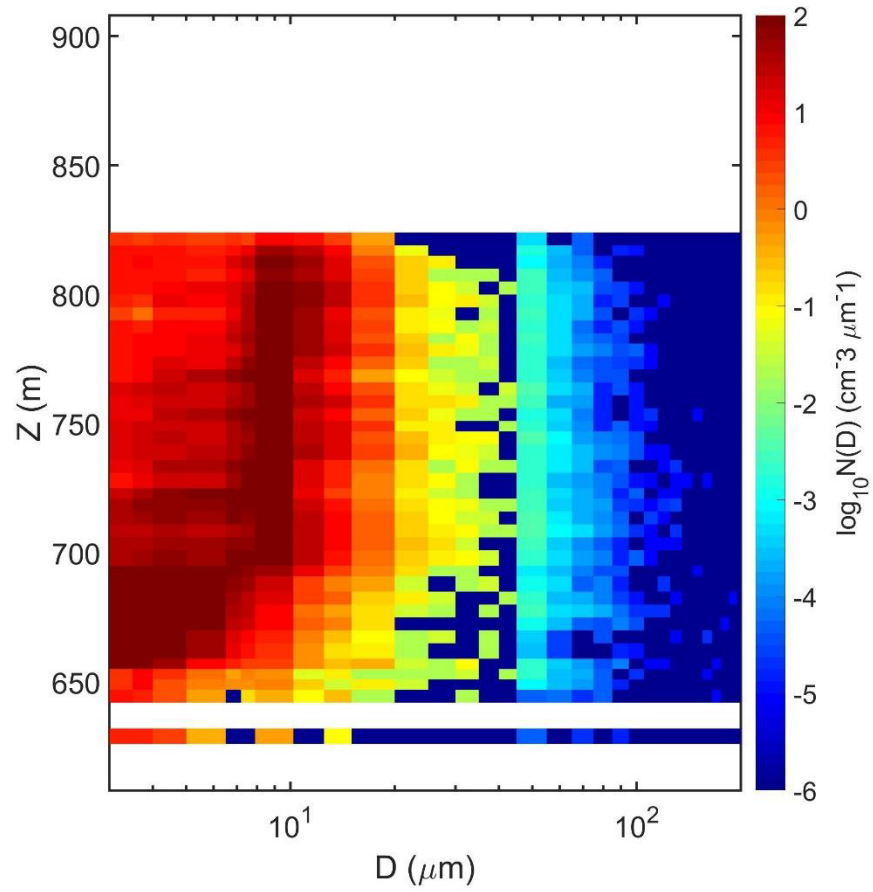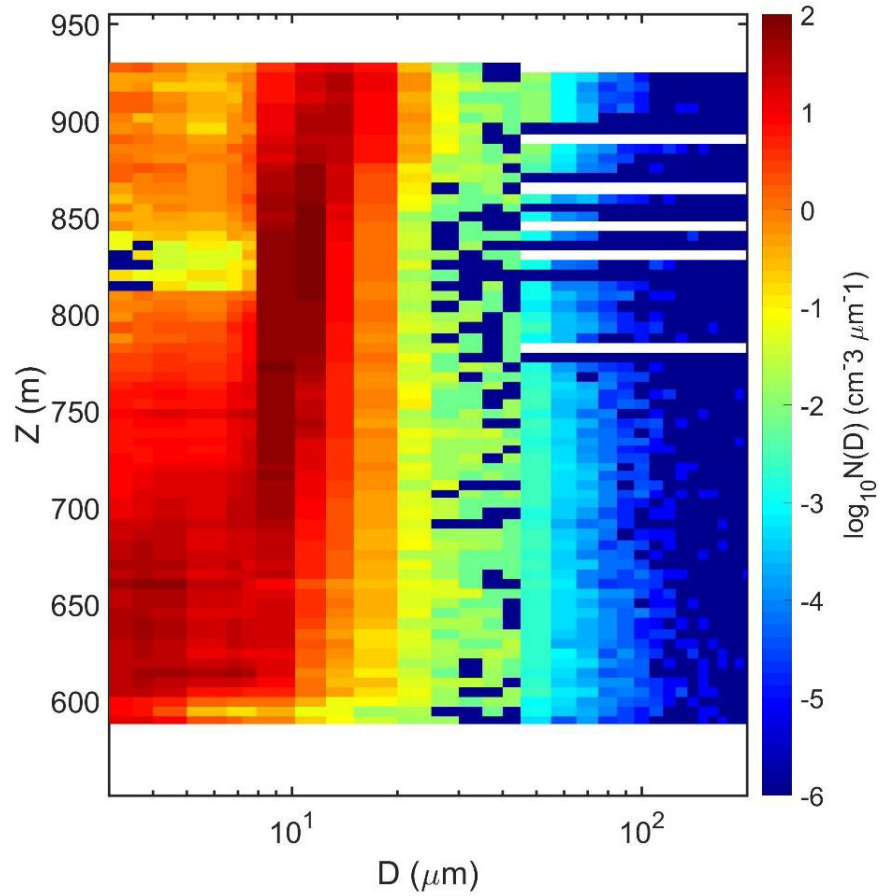
Figure 24: Droplet size distribution for 3 < D < 500 μm as a function of Z for P1 from PRF05, colored by the logarithm of the number distribution function for each size bin.

Figure 25: Droplet size distribution for 3 < D < 500 µm as a function of Z for P3 from PRF05, colored by the logarithm of the number distribution function for each size bin.
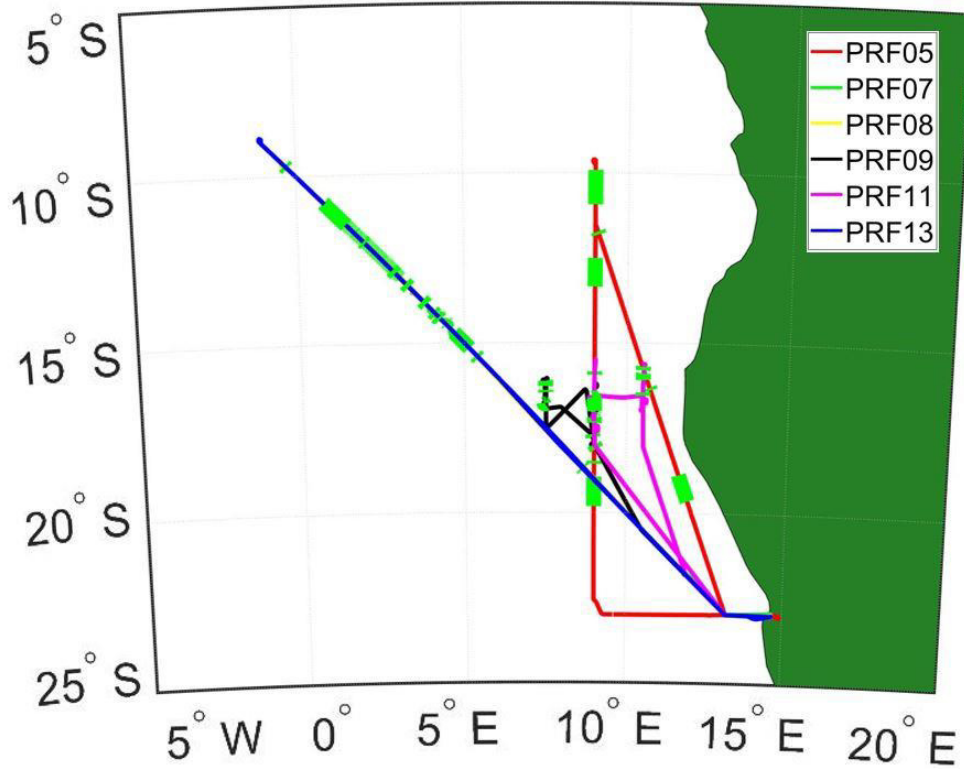
Figure 26: Flight tracks from PRFs 5, 7, 8, 9, 11 and 12 (6, 10, 12, 14, 20 and 25 September 2016), green segments mark the cloud profiles flown (flight tracks from PRFs 7 and 8 coincide with PRF12 and hence are not visible).
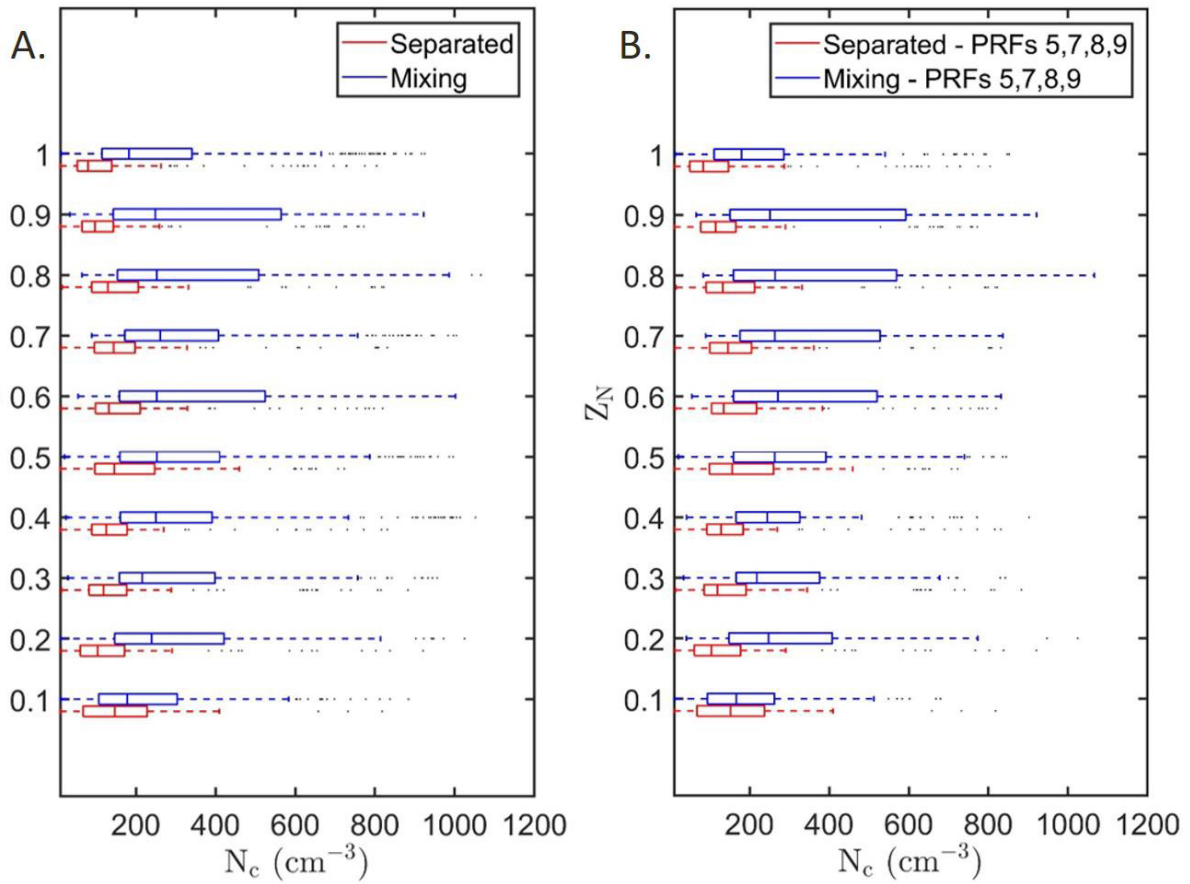
Figure 27: Box and whisker plot for droplet concentration, N_c, measured during cloud profiles flown on (A) PRFs 5, 7, 8, 9, 11 and 13 and (B) PRFs 5, 7, 8 and 9 as a function of the normalized height above cloud base, Z_N, classified based on the two regimes.

Figure 28: Box and whisker plot for effective radius, R_e, measured during cloud profiles flown on (A) PRFs 5, 7, 8, 9, 11 and 13 and (B) PRFs 5, 7, 8 and 9 as a function of the normalized height above cloud base, Z_N, classified based on the two regimes.
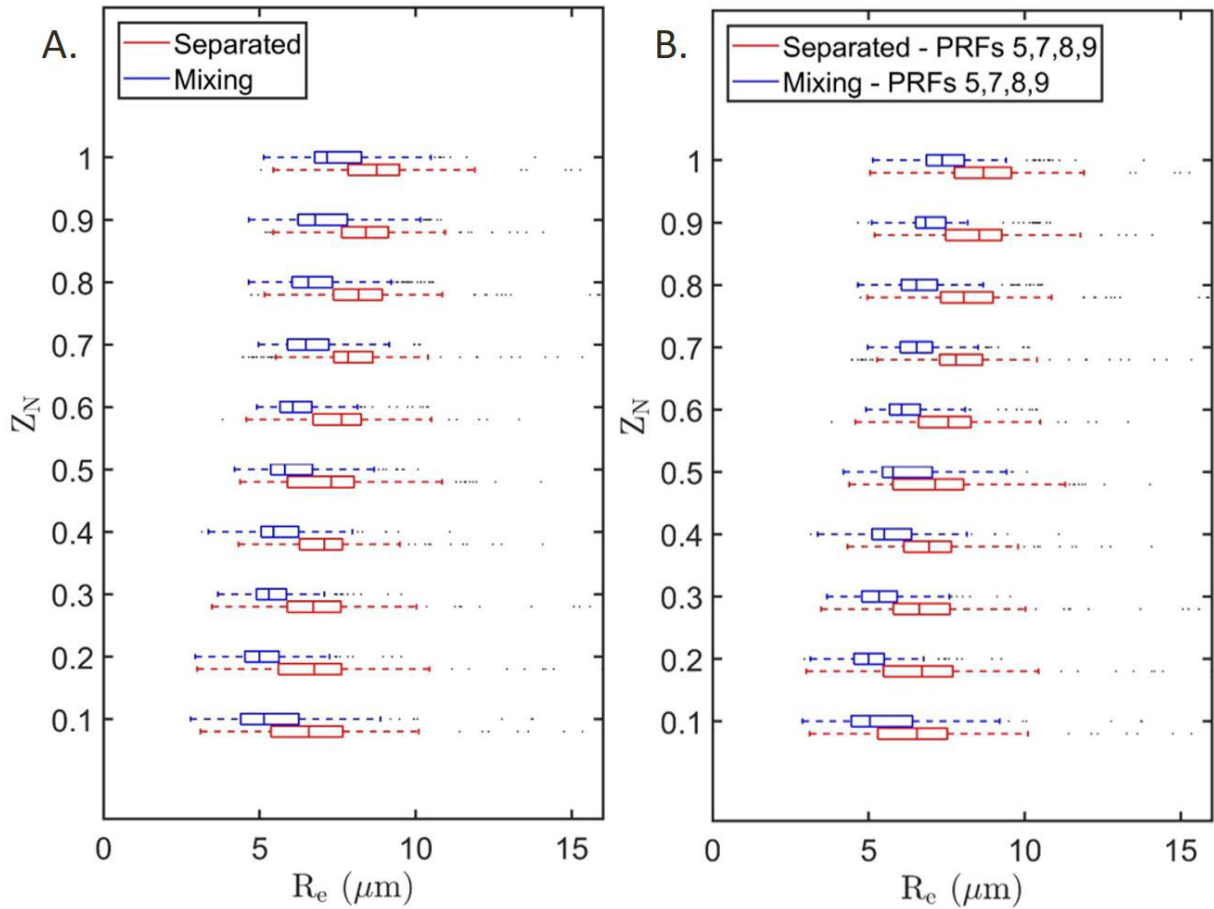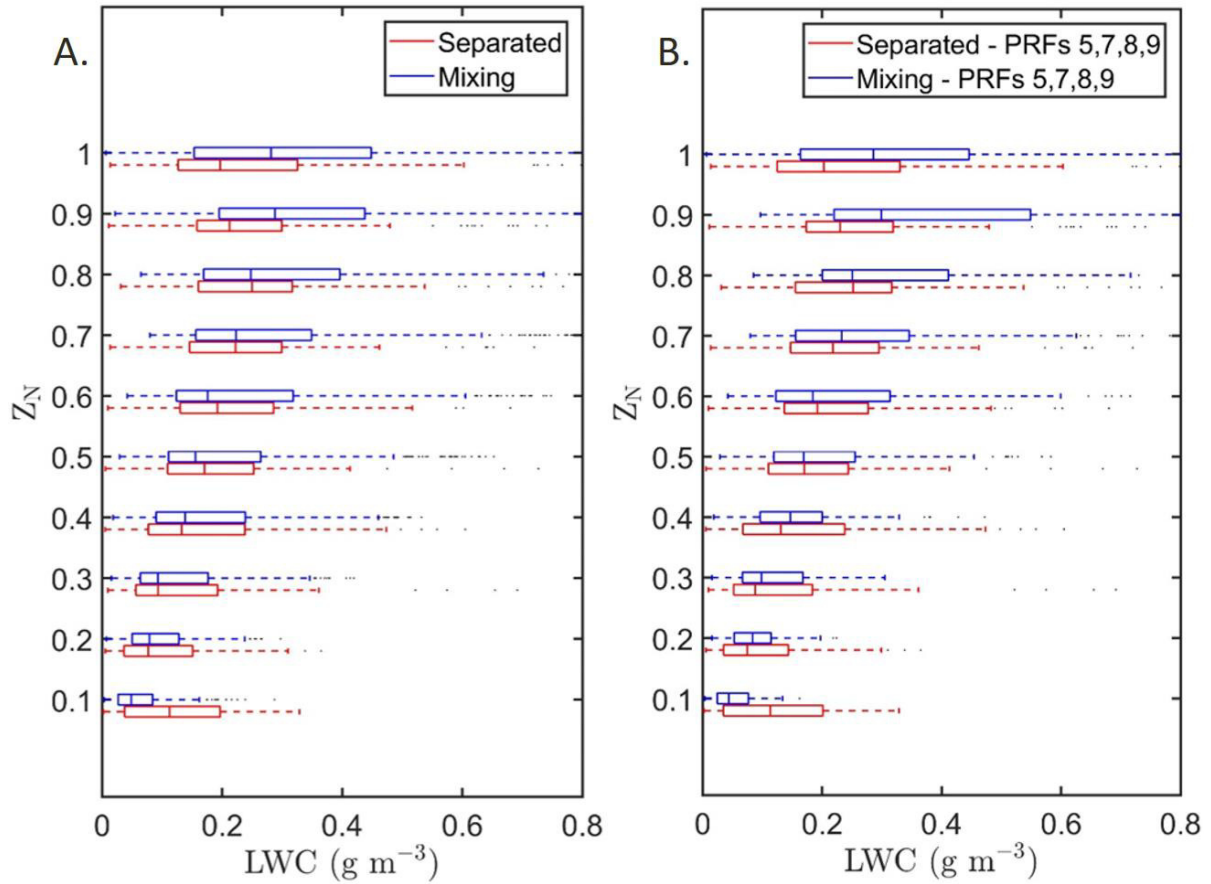
Figure 29: Box and whisker plot for liquid water content, LWC, measured during cloud profiles flown on (A) PRFs 5, 7, 8, 9, 11 and 13 and (B) PRFs 5, 7, 8 and 9 as a function of the normalized height above cloud base, Z_N, classified based on the two regimes.
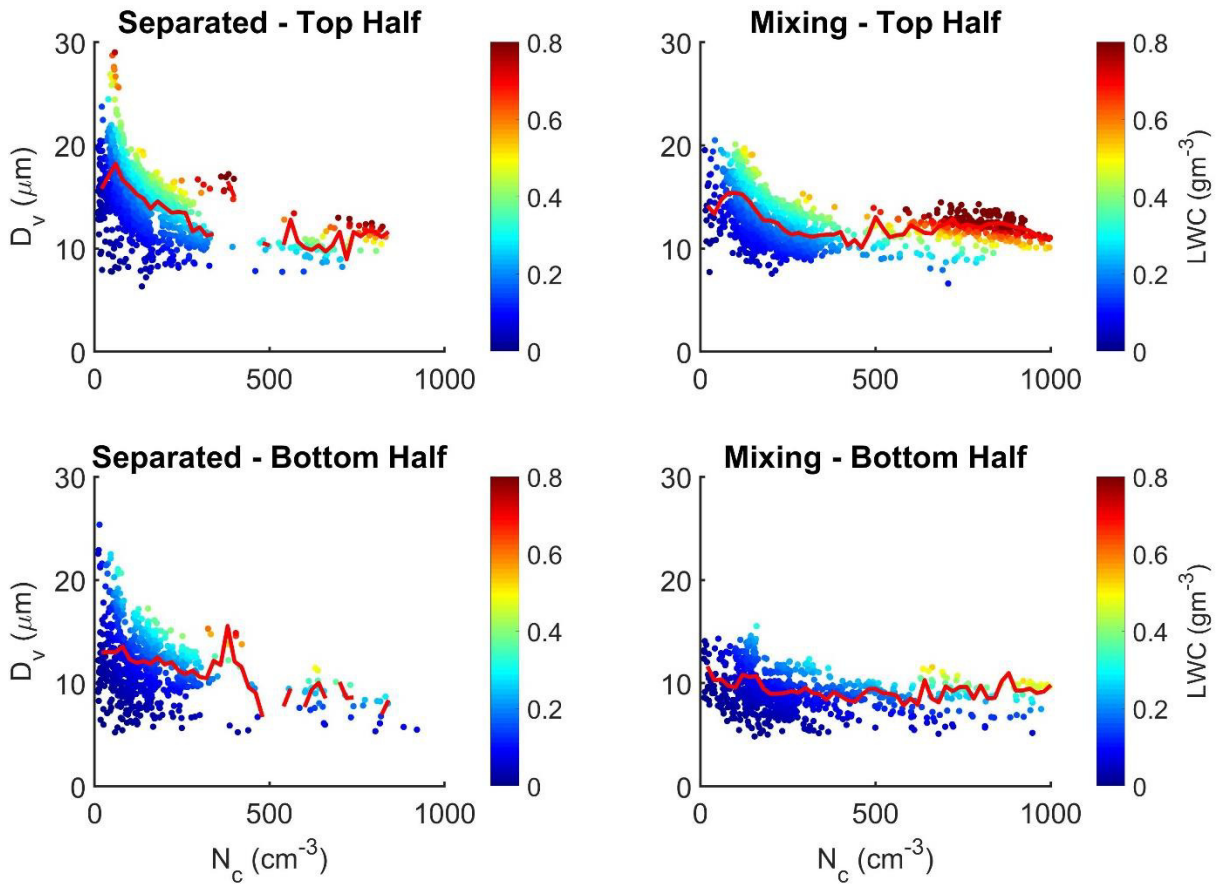
Figure 30: Mean volume diameter (D_v) plotted as a function of N_c, colored by LWC for the top and bottom half of the cloud deck for the separated and mixing regimes, the red line indicates mean D_v as a function of N_c.

Figure 31: Droplet size distribution for 3 < D < 500 µm as a function of Z for S1e from PRF05, colored by the logarithm of the number distribution function for each size bin.
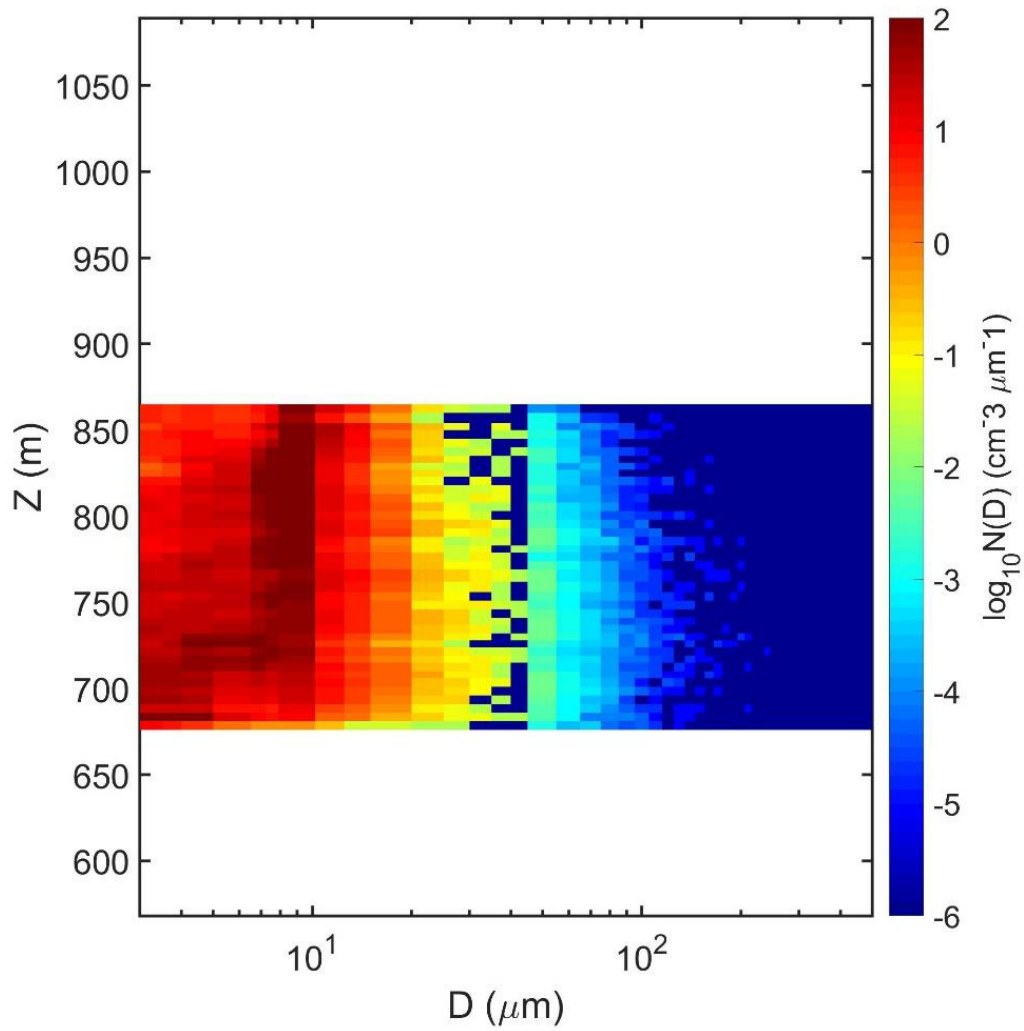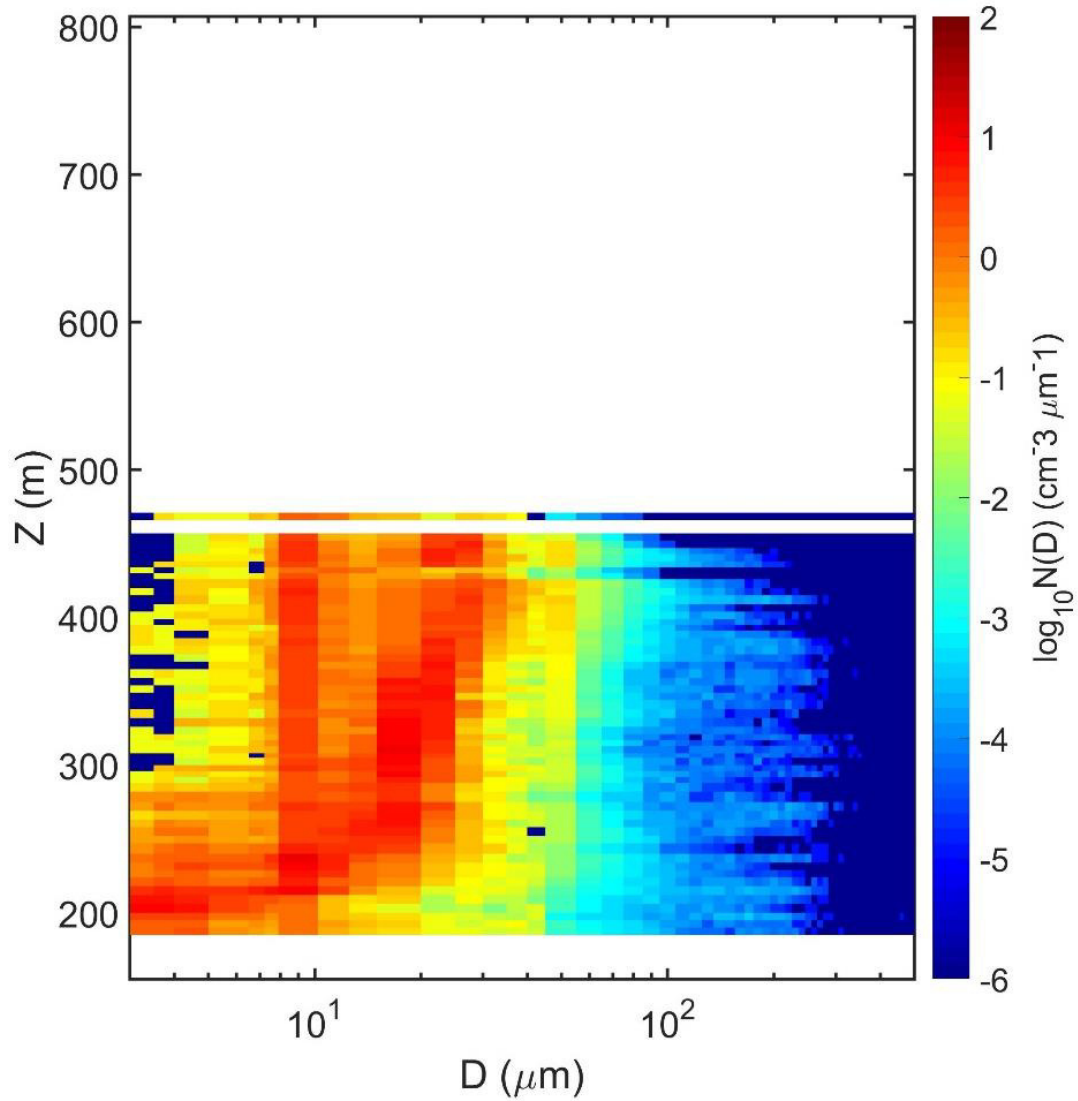
Figure 32: Droplet size distribution for 3 < D < 500 µm as a function of Z for S4e from PRF05, colored by the logarithm of the number distribution function for each size bin.

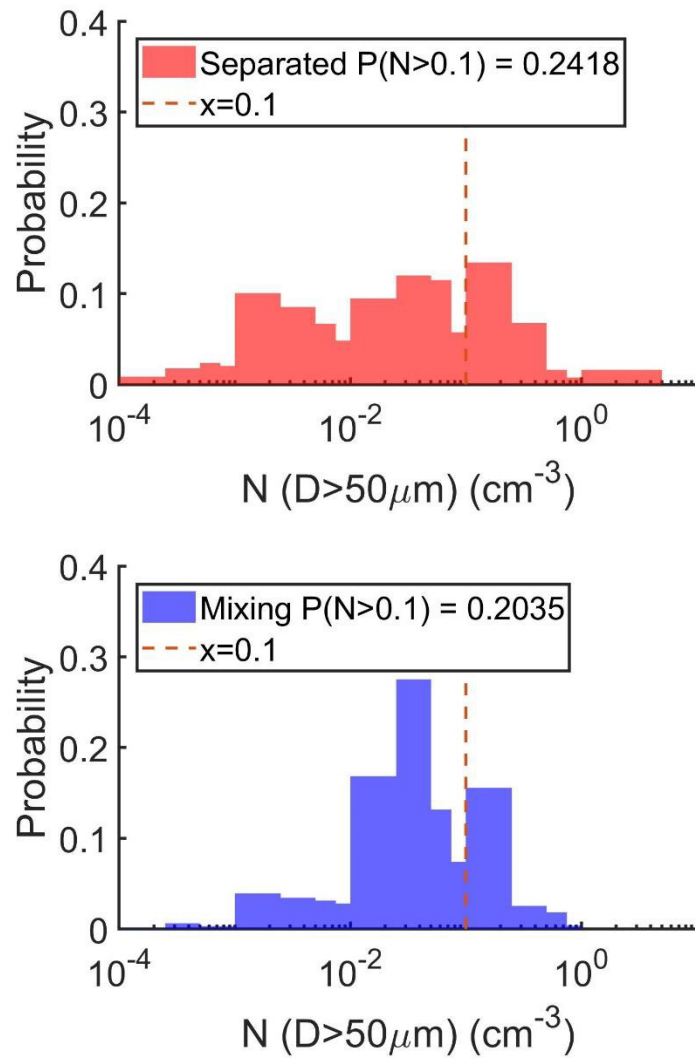Figure 33: Probability distribution for drizzle concentration, N (D>50 µm) for cloud profiles classified into the separated and mixing regimes.

REFERENCES

1. Ackerman, A.S., O.B. Toon, J.P. Taylor, D.W. Johnson, P.V. Hobbs, and R.J. Ferek, 2000: Effects of aerosols on cloud albedo: Evaluation of Twomey's parameterization of cloud susceptibility using measurements of ship tracks. *J. Atmos. Sci.*, **57**, 2684-2695, doi:10.1175/1520-0469(2000)057<2684:EOAOCA>2.0.CO;2.

2. Ackerman, A.S., M.P. Kirkpatrick, D.E. Stevens, and O.B. Toon, 2004: The impact of humidity above stratiform clouds on indirect aerosol climate forcing. *Nature*, **432**, 1014-1017, doi:10.1038/nature03174.

3. Afchine, A. and Coauthors, 2017: Ice particle sampling from aircraft – influence of the probing position on the ice water content. *Atmos. Meas. Technol.*, in review, https://doi.org/10.5194/amt-2017-373

4. Albrecht, B., 1989: Aerosols, Cloud Microphysics, and Fractional Cloudiness, *Science*, **245**, 1227–1230.

5. Baumgardner, D., H. Jonsson, W. Dawson, D. O'Connor, and R. Newton, 2001: The cloud, aerosol and precipitation spectrometer (CAPS): A new instrument for cloud investigations. *Atmos. Res*, **59-60,** 251–264.

6. Baumgardner, D., and Coauthors, 2017: Cloud Ice Properties: In Situ Measurement Challenges. *Meteor. Monogr.*, No. 58, Amer. Meteor. Soc., 9.1-9.23.

7. Biter, C. J., J. E. Dye, D. Huffman, and W. D. King, 1987: The drop-size response of the CSIRO liquid water probe. *J. Atmos. Oceanic Technol.,* **4,** 359–367.

8. Boucher, O., and Coauthors, 2013: Clouds and Aerosols. In: Climate Change 2013: The Physical Science Basis. Contribution of Working Group I to the Fifth Assessment Report of the Intergovernmental Panel on Climate Change [Stocker, T.F., D. Qin, G.-K. Plattner,

M. Tignor, S.K. Allen, J. Boschung, A. Nauels, Y. Xia, V. Bex and P.M. Midgley (eds.)]. Cambridge University Press, Cambridge, United Kingdom and New York, NY, USA.

9. Bretherton, C. S., R. George, R. Wood, G. Allen, D. Leon, and B. Albrecht, 2010a: Southeast Pacific stratocumulus clouds, precipitation and boundary layer structure sampled along 20S during VOCALS-REx. *Atmos. Chem. Phys.*, **10**, 15 921–15 962.

10. Brioude, J., and Coauthors, 2009: Effect of biomass burning on marine stratocumulus clouds off the California coast. *Atmos. Chem. Phys.*, **9**, 8840–8856.

11. Burnet, F., and J.-L. Brenguier, 2007: Observational study of the entrainment-mixing process in warm convective clouds. *J. Atmos. Sci.*, **64**, 1995–2011.

12. Cai, Y., D. C. Montague, W. Mooiweer-Bryan, and T. Deshler, 2008: Performance characteristics of 456 | MARCH 2015 the ultra high sensitivity aerosol spectrometer for particles between 55 and 800 nm: Laboratory and field studies. *J. Aerosol Sci.*, **39**, 759–769, doi:10.1016/j .jaerosci.2008.04.007

13. Chand, D., R. Wood, T.L. Anderson, S.K. Satheesh, and R.J. Charlson, 2009: Satellite-derived direct radiative effect of aerosols dependent on cloud cover, *Nature Geoscience*, **2**, 181-184, doi:10.1038/ngeo437.

14. Coakley, J. A. J., and C. D. Walsh, 2002: Limits to the aerosol indirect radiative effect derived from observations of ship tracks. *J. Atmos. Sci.*, **59**, 668–680.

15. Coddington, O. M., P. Pilewskie, J. Redemann, S. Platnick, P. B. Russell, K. S. Schmidt, W. J. Gore, J. Livingston, G. Wind, and T. Vukicevic, 2010: Examining the impact of overlying aerosols on the retrieval of cloud optical properties from passive remote sensing. *J. Geophys. Res.*, **115**, D10211, doi:10.1029/2009JD012829.

16. Comstock, K., C. S. Bretherton, and S. Yuter, 2005: Mesoscale variability and drizzle in southeast Pacific stratocumulus. *J. Atmos. Sci.*, **62**, 3792–3807.

17. Costantino, L. and Bréon, F. M. 2013. Aerosol indirect effect on warm clouds over South-East Atlantic, from co-located MODIS and CALIPSO observations. *Atmos. Chem. Phys.*, **13**, 69–88.

18. Delene, D. J., 2011: Airborne Data Processing and Analysis Software Package, *Earth Science Informatics*, **4(1)**, 29-44.

19. Durkee, P. A., and Coauthors,. 2000: The impact of ship-produced aerosols on the microstructure and albedo of warm marine stratocumulus clouds: A test of MAST hypotheses 1i and 1ii. *J. Atmos. Sci*, **57,**2554–2569.

20. Endo, S., A.M. Fridlind, W. Lin, A.M. Vogelmann, T. Toto, A.S. Ackerman, G.M. McFarquhar, R.C. Jackson, H.H. Jonsson, and Y. Liu, 2015: RACORO continental boundary layer cloud investigations. Part II: Large-eddy simulations of cumulus clouds and evaluation with in-situ and ground-based observations. *J. Geophys. Res.*, **120**, 5993-6014, doi:10.1002/2014JD022525.

21. Field, P. R., R. Wood, P. R. A. Brown, P. H. Kaye, E. Hirst, R. Greenaway, and J. A. Smith, 2003: Ice particle interarrival times measured with a fast FSSP. *J. Atmos. Oceanic Technol.*, **20**, 249–261, doi:10.1175/1520-0426(2003)020,0249:IPITMW.2.0.CO;2.

22. Field, P.R., A. J. Heymsfield, and A. Bansemer, 2006: Shattering and particle interarrival times measured by optical array probes in ice clouds. *J. Atmos. Oceanic Technol.*, **23**, 1357–1370, doi:10.1175/JTECH1922.1.

23. Hansen, J., M. Sato, and R. Ruedy, 1997: Radiative forcing and climate response. *J. Geophys. Res.*, **102**, 6831-6864, doi:10.1029/96JD03436.

24. Hartmann, D. L., M. Ockert-Bell, and M. Michelsen, 1992: The effect of cloud type on Earth's energy balance: Global analysis. *J. Climate*, **5,** 1281–1304.

25. Haywood, J. M., S.R. Osborne, and S.J. Abel, 2004: The effect of overlying absorbing aerosol layers on remote sensing retrievals of cloud effective radius and cloud optical depth. *Q.J.R. Meteorol. Soc.*, **130**, 779–800. doi: 10.1256/qj.03.100.

26. Haywood, J. M., and K. P. Shine, 1997: Multi-spectral calculations of the direct radiative forcing of tropospheric sulphate and soot aerosols using a column model. *Quart. J. Roy. Meteor. Soc.*, **123**, 1907–1930.

27. Heymsfield, A.J. and G. M. McFarquhar, 1996: High albedos of cirrus in the tropical Pacific warm pool: Microphysical interpretations from CEPEX and from Kwajalein, Marshall Islands. *J. Atmos. Sci.*, **53**, 2424–2451, doi:10.1175/1520-0469(1996)053,2424: HAOCIT.2.0.CO;2.

28. Hill, A. A., S. Dobbie, and Y. Yin, 2008: The impact of aerosols on non-precipitating marine stratocumulus: Part 1. Model description and prediction of the indirect effect. *Quart. J. Roy. Meteor. Soc.*, **134,** 1143–1154.

29. Johnson, B. T., K.P. Shine, and P.M. Forster, 2004: The semi-direct aerosol effect: Impact of absorbing aerosols on marine stratocumulus. *Q.J.R. Meteorol. Soc.*, **130**, 1407–1422. doi: 10.1256/qj.03.61

30. Johnson, B., and Coauthors, 2012: In situ observations of volcanic ash clouds from the FAAM aircraft during the eruption of Eyjafjallajokull in 2010, *J. Geophys. Res. Atmos.*, **117**, D00u24, doi:10.1029/2011jd016760.

31. King, W.D., D. A. Parkin, and R. J. Handsworth, 1978: A hot-wired liquid water device having fully calculable response characteristics. *J. Appl. Meteor.*, **17**, 1809–1813, doi:10.1175/1520-0450(1978)017,1809:AHWLWD.2.0.CO;2.

32. Koch, D. and A. D. Del Genio, 2010: Black carbon semi-direct effects on cloud cover: review and synthesis, *Atmos. Chem. Phys.*, **10**, 7685-7696, doi:10.5194/acp-10-7685-2010.

33. Koren, I., Y. J. Kaufman, D. Rosenfeld, L. A. Remer, and Y. Rudich, 2005: Aerosol invigoration and restructuring of Atlantic convective clouds. *Geophys. Res. Lett.*, **32.**L14828, doi:10.1029/2005GL023187.

34. Korolev, A. V., 2007: Reconstruction of the sizes of spherical particles from their shadow images. Part I: Theoretical considerations. *J. Atmos. Oceanic Technol.*, **24**, 376–389, doi:10.1175/JTECH1980.1.

35. Lance, S. C. A. Brock, D. Rogers, and J. A. Gordon, 2010: Water droplet calibration of the cloud droplet probe (CDP) and inflight performance in liquid, ice and mixed-phase clouds during ARCPAC. *Atmos. Meas. Tech.*, **3**, 1683–1706, doi:10.5194/amt-3-1683-2010.

36. Lawson, R. P., R. E. Stewart, and L. J. Angus, 1998: Observations and numerical simulations of the origin and development of very large snowflakes. *J. Atmos. Sci.*, **55**, 3209–3229, doi:10.1175/1520-0469(1998)055,3209:OANSOT.2.0.CO;2.

37. Lawson, R.P., D. O'Connor, P. Zmarzly, K. Weaver, B. A. Baker, Q. Mo, and H. Jonsson, 2006: The 2DS (stereo) probe: Design and preliminary tests of a new airborne, high speed, high resolution particle imaging probe. *J. Atmos. Oceanic Technol.*, **23**, 1462–1471, doi:10.1175/JTECH1927.1

38. Lehmann, K., H. Siebert, and R. A. Shaw, 2009: Homogeneous and inhomogeneous mixing in cumulus clouds: Dependence on local turbulence structure. *J. Atmos. Sci.*, **66**, 3641–3659, doi:10.1175/2009JAS3012.1.

39. Lohmann, U., and J. Feichter, 2005: Global indirect aerosol effects: A review. *Atmos. Chem. Phys.*, **5**, 715–737.

40. Lu, C., Y. Liu, and S. Niu, 2011: Examination of turbulent entrainment-mixing mechanisms using a combined approach. *J. Geophys. Res.*, **116**, D20207, doi:10.1029/2011JD015944.

41. Marshak, A., G. Wen, J. A. Coakley, L. A. Remer, N. G. Loeb, and R. F. Cahalan, 2008: A simple model for the cloud adjacency effect and the apparent bluing of aerosols near clouds, *J. Geophys. Res.*, **113**, D14S17, doi:10.1029/2007JD009196

42. McFarquhar, G. M. and H. Wang, 2006: Effects of aerosols on trade wind cumuli over the Indian Ocean: Model simulations. *Q.J.R. Meteorol. Soc.*, **132**, 821–843. doi: 10.1256/qj.04.179

43. McFarquhar, G. M., and A. J. Heymsfield, 2001: Parameterizations of INDOEX microphysical measurements and calculations of cloud susceptibility: Applications for climate studies, *J. Geophys. Res.*, **106(D22)**, 28675–28698, doi:10.1029/2000JD900777.

44. McFarquhar, G. M., G. Zhang, M. R. Poellot, G. L. Kok, R. McCoy, T. Tooman, A. Fridlind, and A. J.Heymsfield, 2007: Ice properties of single-layer stratocumulus during the Mixed-Phase Arctic Cloud Experiment: 1. Observations. *J. Geophys. Res.*, **112**, D24201, doi:10.1029/2007JD008633.

45. McFarquhar, G. M., and Coauthors, 2017: Processing of ice cloud in situ data collected by bulk water, scattering, and imaging probes: Fundamentals, uncertainties, and efforts

toward consistency. Ice Formation and Evolution in Clouds and Precipitation: Measurement and Modeling Challenges, Meteor. Monogr., No. 58, Amer. Meteor. Soc., doi:10.1175/AMSMONOGRAPHS-D-16-0007.1.

46. Morrison, H., and W. W. Grabowski, 2011: Cloud system-resolving model simulations of aerosol indirect effects on tropical deep convection and its thermodynamic environment. *Atmos. Chem. Phys.*, **11**, 10 503–10 523, doi:https://doi.org/10.5194/acp-11-10503-2011.

47. Painemal, D., and P. Zuidema, 2011: Assessment of MODIS cloud effective radius and optical thickness retrievals over the southeast Pacific with VOCALS-REx in situ measurements. *J. Geophys. Res.*, **116**, D24206, doi:10.1029/2011JD016155.

48. Ramanathan, V., and Coauthors, 2001: Indian Ocean Experiment: An integrated analysis of the climate forcing and effects of the great Indo-Asian haze, *J. Geophys. Res.,* **106**, 28371–28398, doi:10.1029/2001JD900133.

49. Ramaswamy, V., and Coauthors, 2001: Radiative Forcing of Climate Change, in: Climate Change 2001: The Scientific Basis. Contribution of working group I to the Third Assessment Report of the Intergovernmental Panel on Climate Change, edited by: J. T. Houghton, Y. Ding, D. J. Griggs, M. Noguer, P. J. van der Linden, X. Dai, K. Maskell, and C. A. Johnson, pp. 349–416, Cambridge Univ. Press, New York, 2001.

50. Redemann, J., 2014: Observations of aerosols above clouds and their interactions (ORACLES) Proposal. More information about ORACLES available at https://espo.nasa.gov/home/oracles/content/ORACLES.

51. Rosenfeld, D., U. Lohmann, G. B. Raga, C. D. O'Dowd, M. Kulmala, S. Fuzzi, A. Reissell, and M. O. Andreae, 2008a: Flood or drought: How do aerosols affect precipitation?, *Science*, **321**, 1309–1313.

52. Rosenfeld, D., H. Wang, and P. J. Rasch, 2012a: The roles of cloud drop effective radius and LWP in determining rain properties in marine stratocumulus, *Geophys. Res. Lett.*, **39**, L13801, doi:10.1029/2012GL052028

53. Rosenfeld, D., and Coauthors, 2014: Global observations of aerosol-cloud-precipitation climate interactions, *Rev. Geophys.*, **52**, 750–808, doi:10.1002/2013RG000441.

54. Sandu, I., J.-L. Brenguier, O. Geoffroy, O. Thouron, and V. Masson, 2008: Aerosol impacts on the diurnal cycle of marine stratocumulus. *J. Atmos. Sci.*, **65**, 2705–2718, doi:https://doi.org/10.1175/2008JAS2451.1.

55. Small, J. D., P. Y. Chuang, G. Feingold, and H. Jiang, 2009: Can aerosol decrease cloud lifetime? *Geophys. Res. Lett.*, **36**, L16806, doi:10.1029/2009GL038888

56. Stein, A.F., Draxler, R.R, Rolph, G.D., Stunder, B.J.B., Cohen, M.D., and Ngan, F., (2015). NOAA's HYSPLIT atmospheric transport and dispersion modeling system, *Bull. Amer. Meteor. Soc*., **96**, 2059-2077, http://dx.doi.org/10.1175/BAMS-D-14-00110.1

57. Stevens, B., and G. Feingold, 2009: Untangling aerosol effects on clouds and precipitation in a buffered system. *Nature*, **461** (7264), 607–613.

58. Strapp, J. W., W. R. Leaitch, and P. S. K. Liu, 1992: Hydrated and dried aerosol-size-distribution measurements from the Particle Measurement Systems FSSP-300 probe and the deiced PCASP100X probe. *J. Atmos. Oceanic Technol.*, **9**, 548–555.

59. Strapp, J.W., and Coauthors, 2003: Wind tunnel measurements of the response of hot-wire liquid water content instruments to large droplets. *J. Atmos. Oceanic Technol.*, **20**, 791–806.

60. Terai, C. R., R. Wood, D.C. Leon, and P. Zuidema, 2012: Does precipitation susceptibility vary with increasing cloud thickness in marine stratocumulus?, *Atmos. Chem. Phys.*, **12**, 4567-4583, https://doi.org/10.5194/acp-12-4567-2012.

61. Twohy, C. H., M. D. Petters, J. R. Snider, B. Stevens, W. Tahnk, M. Wetzel, L. Russell, and F. Burnet, 2005: Evaluation of the aerosol indirect effect in marine stratocumulus clouds: Droplet number, size, liquid water path, and radiative impact. *J. Geophys. Res.*, **110**, D08203, doi:10.1029/2004JD005116

62. Twomey, S., Pollution and the planetary albedo, *Atmos. Environ.*, **8**, 1251-1256, 1974.

63. Twomey, S., The influence of pollution on the shortwave albedo of clouds*, J. Atmos. Sci.*, **34**, 1149–1152, 1977.

64. Warren, S. G., C. J. Hahn, J. London, R. M. Chervin, and R. L. Jenne, 1988: Global distribution of total cloud cover and cloud types over ocean. NCAR Tech. Note NCAR/TN-317+STR, National Center for Atmospheric Research, Boulder, CO, 42 pp. + 170 maps.

65. Weigel, R., and Coauthors, 2016: Thermodynamic correction of particle concentrations measured by underwing probes on fast-flying aircraft. *Atmos. Meas. Tech.*, **9**, 5135–5162, doi:10.5194/amt-9-5135-2016.

66. Wen, G., A. Marshak, and R. F. Cahalan, 2008: Importance of molecular Rayleigh scattering in the enhancement of clear sky reflectance in the vicinity of boundary layer cumulus clouds, *J. Geophys. Res.*, **113**, D24207, doi:10.1029/2008JD010592.

67. Wood, R., 2005a: Drizzle in stratiform boundary layer clouds. Part I: Vertical and horizontal structure. *J. Atmos. Sci.*, **62**, 3011–3033.